Neuron

Article

Optogenetic fUSI for brain-wide mapping of neural activity mediating collicular-dependent behaviors

Graphical abstract

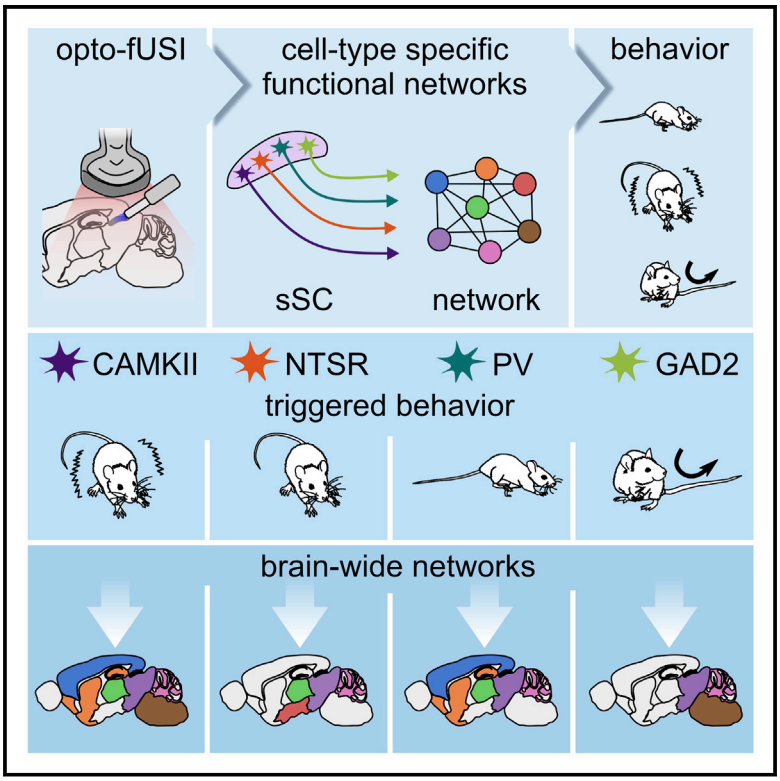

Authors

Arnau Sans-Dublanc, Anna Chrzanowska, Katja Reinhard, ..., Gabriel Montaldo, Alan Urban, Karl Farrow

Correspondence

karl.farrow@nerf.be

In brief

Combining optogenetics and functional ultrasound imaging Sans-Dublanc et al. showed that distinct, partially overlapping brain-wide functional networks are activated by different collicular cell types to generate a variety of behaviors. This approach allows one to observe the whole-brain networks downstream of individual cell types in an unbiased manner.

Highlights

- Opto-fUSI enables whole-brain analysis of functional connectivity
- Collicular cell types activate distinct brain-wide networks and behaviors
- Opto-fUSI revealed novel brain areas involved in collicular behaviors

Sans-Dublanc et al., 2021, Neuron *109*, 1888–1905
June 2, 2021
https://doi.org/10.1016/j.neuron.2021.04.008

CellPress

CellPress

Neuron

Article

Optogenetic fUSI for brain-wide mapping of neural activity mediating collicular-dependent behaviors

Arnau Sans-Dublanc,[1,2,7] Anna Chrzanowska,[1,2,7] Katja Reinhard,[1,2,3] Dani Lemmon,[1,6] Bram Nuttin,[1,2] Théo Lambert,[1,4,5] Gabriel Montaldo,[1,4] Alan Urban,[1,2,3,5] and Karl Farrow[1,2,3,8,*]

[1]Neuro-Electronics Research Flanders, Leuven, Belgium
[2]Department of Biology, KU Leuven, Leuven, Belgium
[3]VIB, Leuven, Belgium
[4]imec, Leuven, Belgium
[5]Department of Neurosciences, KU Leuven, Leuven, Belgium
[6]Faculty of Pharmaceutical, Biomedical, and Veterinary Sciences, University of Antwerp, Antwerp, Belgium
[7]These authors contributed equally
[8]Lead contact
*Correspondence: karl.farrow@nerf.be
https://doi.org/10.1016/j.neuron.2021.04.008

SUMMARY

Neuronal cell types are arranged in brain-wide circuits that guide behavior. In mice, the superior colliculus innervates a set of targets that direct orienting and defensive actions. We combined functional ultrasound imaging (fUSI) with optogenetics to reveal the network of brain regions functionally activated by four collicular cell types. Stimulating each neuronal group triggered different behaviors and activated distinct sets of brain nuclei. This included regions not previously thought to mediate defensive behaviors, for example, the posterior paralaminar nuclei of the thalamus (PPnT), which we show to play a role in suppressing habituation. Neuronal recordings with Neuropixels probes show that (1) patterns of spiking activity and fUSI signals correlate well in space and (2) neurons in downstream nuclei preferentially respond to innately threatening visual stimuli. This work provides insight into the functional organization of the networks governing innate behaviors and demonstrates an experimental approach to explore the whole-brain neuronal activity downstream of targeted cell types.

INTRODUCTION

Different behavioral tasks rely on distinct networks of neurons distributed across the brain. Insights into how specific cell types are linked to sensation and behavior have made some great advances through the application of molecular technologies, providing a list of critical circuit elements (Zeng and Sanes, 2017). Computational understanding has been gained by comparing large-scale measurements of neuronal activity with sensory inputs and behavior (Ahrens et al., 2012; Aimon et al., 2019; Steinmetz et al., 2019; Stringer et al., 2019). However, in mammals, the link between individual cell types, large-scale neuronal activity, and behavior remains unclear. In the superior colliculus (SC), there is evidence for a strong relationship between individual cell types and behavior (Hoy et al., 2019; Masullo et al., 2019; Shang et al., 2015, 2018; Zhang et al., 2019). Here, we use this relationship to study both the cell-type-specific contributions to behavior and the brain-wide functional networks that lie downstream of these same collicular populations.

In mice, the SC is a major hub of visual processing. Its superficial layers contain a set of genetically identified cell types, with distinct anatomy and visual response properties, that project to a set of targets that drive orienting and avoidance behaviors (Gale and Murphy, 2014, 2018; Inayat et al., 2015; Whyland et al., 2020). The optogenetic activation of some of these cell types has provided insight into the relationship between individual output circuits of the SC and behavior, in which activation of pulvinar projecting neurons trigger arrest behaviors, and activation of neurons projecting to the parabigeminal nucleus (PBG) leads to flight behavior (Shang et al., 2018; Wei et al., 2015). These optogenetically induced behaviors resemble the responses of mice to visual stimuli that mimic avian predators (De Franceschi et al., 2016; Yilmaz and Meister, 2013).

Combinations of cell-type-specific stimulation and whole-brain recordings using functional magnetic resonance imaging (fMRI) have provided insights into the relationship between cell types and brain-wide network activity (Lee et al., 2016; Nakamura et al., 2020). However, recording techniques such as fMRI suffer from limited resolution, which makes it difficult to clearly assign activity to small brain nuclei, in particular, in small mammals (Bernal-Casas et al., 2017; Lee et al., 2016). Functional ultrasound imaging (fUSI) has been developed to study brain-wide activation patterns at a spatial and temporal resolution in awake mice, which makes it practical to follow neural activity

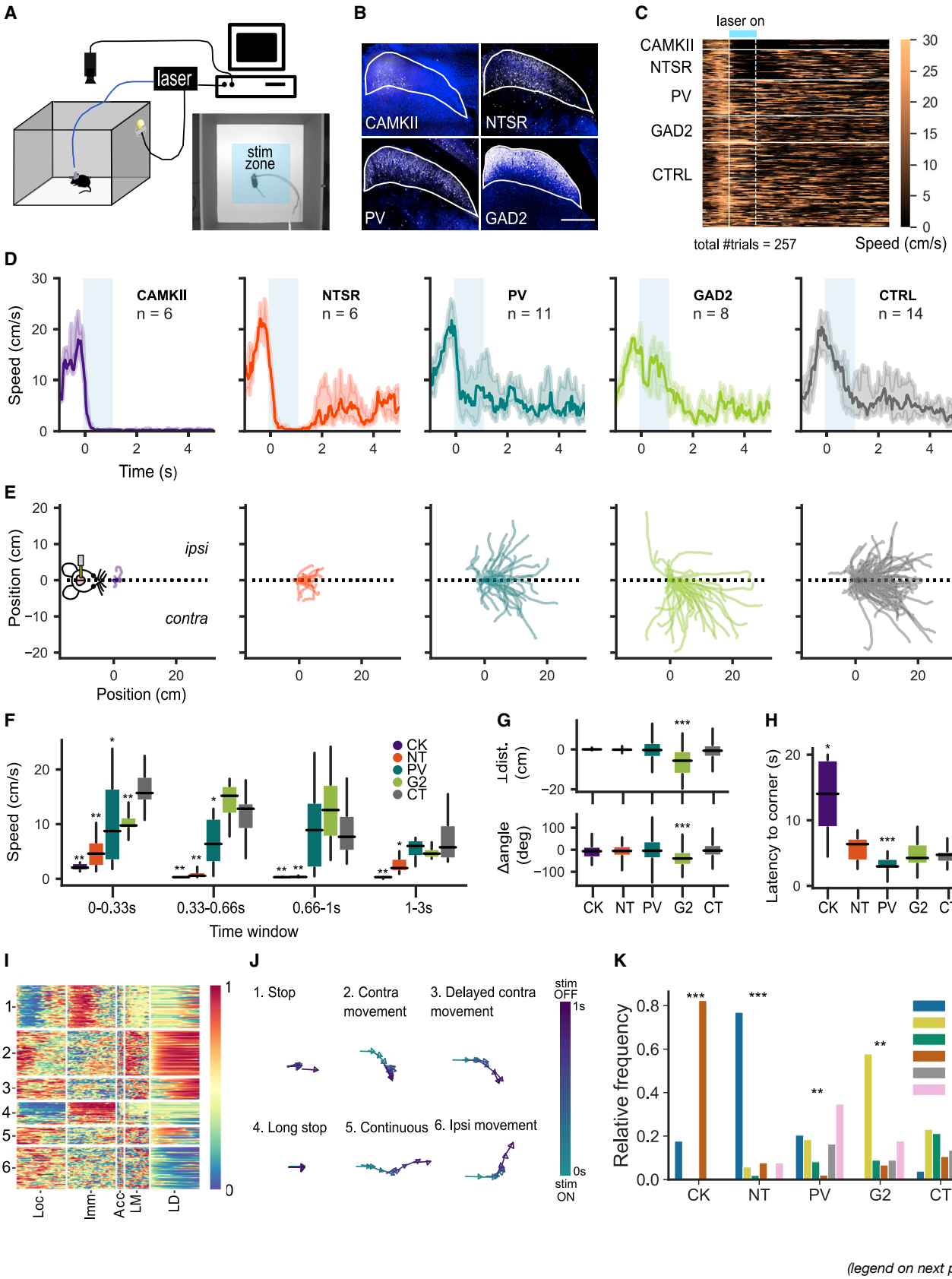

(legend on next page)

in most nuclei of the brain at a resolution of ~100 μm^3 (Brunner et al., 2020; Macé et al., 2011, 2013, 2018; Rabut et al., 2019).

By combining fUSI with optogenetics (opto-fUSI), we reveal the neural networks through which information is routed after the activation of different cell types in the SC. We unravel the differences in the spatial and temporal organization of cell-type-dependent network activation, which we find to be consistent with differences in evoked behaviors. Opto-fUSI allows us to identify new brain areas that link sensory inputs to behavioral output. Finally, chemogenetic manipulations reveal the potential function of one newly identified group of nuclei, the posterior paralaminar nuclei of the thalamus (PPnT), in visually triggered behaviors.

RESULTS

Different collicular cell types trigger different innate behaviors

To understand the contributions that different collicular cell types make to behavior, we optogenetically activated 4 cell populations: (1) excitatory neurons expressing calcium/calmodulin-dependent protein kinase type II (CAMKII or CK); (2) neurotensin receptor 1-expressing neurons (NTSR or NT); (3) parvalbumin-expressing neurons (PV); and (4) inhibitory neurons expressing glutamic acid decarboxylase 2 (GAD2 or G2). We restricted the expression of channelrhodopsin2 (ChR2) to different cell classes by crossing Cre-expressing transgenic mouse lines (NTSR-GN209-Cre, PV-Cre, and GAD2-Cre) with a ChR2-reporter mouse line or by injecting an adeno-associated virus (AAV) for labeling CAMKII neurons (see Method details). Histological analysis confirmed the layer specificity and partial overlap of different cell types (Figures 1 and S1). CAMKII and NTSR neurons had the highest overlap (NTSR-CAMKII = 64.97%, interquartile range [IQR] = 60.92–69.01), in contrast to PV and GAD2 neurons that had little overlap with other populations (PV-GAD2 = 12.67%, IQR = 9.45–15.9).

We tested the behavioral effect of optogenetically stimulating each cell type in freely moving animals (Figure 1; Video S1). The stimulus consisted of blue light pulses of either a high-frequency (1 s, 20 Hz, or 50 Hz) or low-frequency (4 s, 5 Hz) optical stimulation. Activation of each neural population led to distinct behavioral effects, which ranged from stopping (CAMKII and NTSR neurons) to directed movement (PV and GAD2 neurons). Unlike the control group, the experimental groups responded with a steep drop in speed during the first 333 ms after stimulus onset (Figures 1C, 1D, and 1F). The activation of CAMKII neurons evoked long stopping events (duration 9.21 s, IQR = 8.02–12.65; Figure S1G), whereas the stimulation of NTSR neurons induced stopping during the stimulus (duration 1.69 s, IQR = 1.42–1.95; Figure S1G). The activation of PV cells caused mice to slow down, but rarely led to a full stop (Figure S1H). Instead, they actively moved toward a corner (Figure 1H). Stimulation of GAD2 neurons generated either rotational movement (median Δ angle: −39°, IQR = −70.01 to −9.36; Figures 1F and 1G) or a whole-body drift contralateral to the stimulated hemisphere (median perpendicular distance: −5.66 cm, IQR = −12.36 to −0.72; Figure 1G, top).

To analyze the behavior in a less biased manner, the positions of five body landmarks (nose, each ear, and proximal and distal ends of the tail) were tracked to measure and cluster animal movements (Storchi et al., 2020) (see Method details). CAMKII had the highest proportion of long stopping (cluster 4), NTSR had the highest proportion of short stopping (cluster 1), GAD2 had a strong preference for contralateral movements (cluster 2), while PV showed a larger diversity of responses (Figures 1I–1K). These findings suggest that each collicular cell type contributes differentially to behavior.

Brain-wide functional fUSI during optogenetic stimulation in mice

To assess the brain-wide activity that drives the different behaviors observed above, we developed a chronic preparation that allowed us to combine fUSI and optogenetics in awake

Figure 1. Different SC cell types trigger different defensive behaviors

(A) Schematic of the open field setup for optogenetics and a video frame of a mouse entering the stimulation zone (blue rectangular shading).

(B) Coronal section showing expression of ChR2 in distinct cell lines. Scale bar, 500 μm.

(C) Heatmap of mice speeds during optogenetic stimulation obtained from the first experimental sessions. Horizontal white lines separate different mouse lines. Vertical solid and dashed white lines mark stimulus onset and offset, respectively. Light blue bar marks the stimulus duration.

(D) Speed profiles. Each trace represents the median speed for each mouse line. The shaded area represents the interquartile range.

(E) Mice trajectories during the 1-s stimulus. Traces were aligned and rotated by the initial body position angle. CAMKII: n = 6, 14 trials; NTSR: n = 6, 41 trials; PV: n = 11, 50 trials; GAD2: n = 8, 43 trials; CTRL n = 14, 109 trials.

(F) Speed quantification during chosen time windows. (0–0.33 s: CAMKII p = 0.0003, NTSR p = 0.0003, PV p = 0.026, GAD2 p = 0.004; 0.33–0.66 s: CAMKII p = 0.0003, NTSR p = 0.0004, PV p = 0.03, GAD2 p = 0.10; 0.66–1 s: CAMKII p = 0.003, NTSR p = 0.0004, PV p = 0.34, GAD2 p = 0.10; 1–3 s: CAMKII p = 0.0003, NTSR p = 0.007, PV p = 0.38, GAD2 p = 0.18).

(G) Quantification of body position at the stimulation offset, represented as a change of angle (bottom; CAMKII p = 0.26; NTSR p = 0.31; PV p = 0.45; GAD2 p = 0.00002) and perpendicular distance (top; CAMKII p = 0.27; NTSR p = 0.29; PV p = 0.38; GAD2 p = 0.00002), both in reference to x axis (dashed line in E).

(H) Latency of movement to a corner (CAMKII p = 0.003; NTSR p = 0.15; PV p = 0.013; GAD2 p = 0.49). All data points are averaged over mice, except in (G) (averaged over trials). Significance between control and each mouse line was tested using the Mann-Whitney *U* test. Box-and-whisker plots in (F)–(H) show median, interquartile range, and range.

(I) Heatmap of the behavioral responses to stimulation. Each row shows a trial with different measures: locomotion (Loc), immobility (Imm), acceleration (Acc), lateral motility (LM), and lateral distance (LD), separated by vertical white lines. Clusters are separated by horizontal white lines. For LM and LD, 0 and 1 indicate leftward and rightward locomotion, respectively.

(J) Single-trial examples of clusters. Color shading indicates time.

(K) Cluster assignment distributions for each mouse line. Significance between control and each mouse line distribution was tested using Fisher's exact test (CAMKII p = 6.9e−11, NTSR p = 2.2e−16, PV p = 0.0045, GAD2 p = 0.0041).

Alpha = 0.05, *p < 0.05, **p < 0.01, ***p < 0.001.

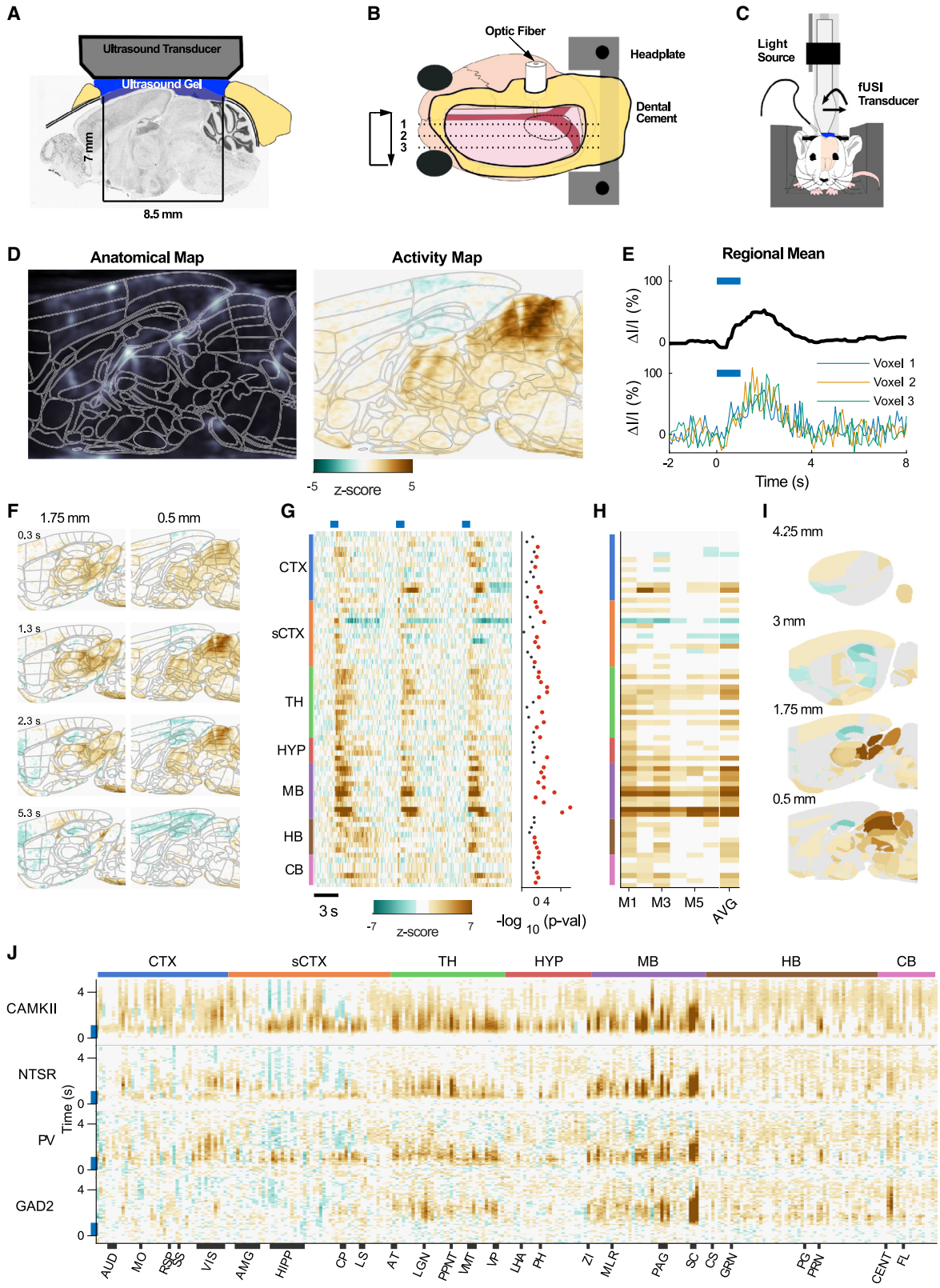

(legend on next page)

head-fixed animals. We performed a large chronic cranial window (AP +2 to −6.5; L +1.25 to −4.5) and implanted an optic fiber at the surface of the ipsilateral SC, near the midline, at an angle of 56° (Figures 2A–2C). Neural activity was monitored with a fUSI transducer positioned over the craniotomy parallel to the long axis of the animal. Sagittal cross-sections were imaged sequentially, as the transducer was stepped (250 μm) along the medial-lateral axis (Figures 2A–2C). While imaging each plane, the colliculus was activated with high-frequency (1 s, 20 Hz, or 50 Hz) and low-frequency (4 s, 5 Hz) optical stimulation. Afterward, each voxel was assigned to an individual brain region by registration to a modified version (Table S1) of the Allen Mouse Brain Common Coordinate Framework version 3 (CCF v3) (Brunner et al., 2020; Lein et al., 2007) (Figure 2D).

To build a spatial map of brain activity, we compared, voxel by voxel, the hemodynamic signals (DI/I, referred to as "activity") obtained during and after the optogenetic stimulus to a baseline (Figures 2D–2F; Video S2). To estimate the response of each region, the hemodynamic activity of all voxels within that area were averaged (Figures 2E and 2G). Temporal traces were obtained for each mouse and compared (t test corrected for false discovery rate) to identify responsive regions (Figures 2G–2I). The average responses for each mouse line are shown in Figure 2J. The same analysis was applied to the low-frequency stimulation data (Figure S2).

To assess whether head-fixed animals display comparable behaviors to freely moving animals, we performed similar experiments with NTSR and GAD2 mice that were head fixed on a spherical treadmill (Figures S3A and S3B). Behavioral and brain activity analysis suggested that the optogenetically evoked behaviors and corresponding brain-wide activity patterns are triggered independently of locomotion (see details in Figure S3). Thus, for the next part of the study, we decided to focus on our restrained preparation (Figure 2) using more extensive craniotomies suitable for imaging a larger portion of the brain with minimal movement artifacts.

Distribution of hemodynamic response properties

We looked at the temporal structure of the hemodynamic changes induced by the optical stimulation (Figure 3). We found that the high-frequency stimulus caused a reliable set of temporal responses that could be grouped into 4 broad categories (see Method details), namely: fast, delayed, slow, and inhibitory (Figures 3A and 3B).

The number of responsive areas and the distribution of the different response types varied among the mouse lines (active areas: CK = 246, NT = 157, PV = 170, G2 = 82). We found that the fast responses were more common in CAMKII and NTSR mice (CK 47%, NT 42%, PV 35%, G2 5%). PV mice had a similar proportion of fast (35%) and delayed (34%) responses, while GAD2 mice had predominantly delayed (45%) and slow (44%) responses. In addition, inhibitory responses were more common in NTSR and PV mice (CK 3%, NT 11%, PV 13%, G2 5%). The distribution of latencies formed two broad groups—those responding within and those responding after the first 2 s (Figure 3C). While the distribution of latencies is similar for CAMKII, NTSR, and PV cell populations, spanning the entire range of latencies, the activation of inhibitory GAD2 neurons did not cause any early responses (Figures 3A and 3D).

Stimulating the SC neurons at a lower frequency (5 Hz for 4 s) generated similar temporal dynamics triggered by each neuronal population (fast, delayed, slow, inhibitory), but exaggerated the differences between them (Figure S4). In addition, the change in frequency corresponded with a reversal in the sign of the response in some areas such as the visual cortex (Figures 3 and S4).

The distribution of the different response types across the major brain structures was relatively consistent between the different cell populations, except for slow responses (Figure 3E). For example, CAMKII and NTSR had the largest proportion of slow responding areas in the cerebellum (23% and 24%, respectively), while GAD2 had none in that structure.

Each collicular cell type modulates a distinct brain-wide network

To understand how the activation of each neuronal population triggers distinct brain-wide networks, we compared the distribution of brain areas that had increased or decreased hemodynamic responses for each cell type. Based on the temporal

Figure 2. Functional ultrasound imaging of awake mice during optogenetic stimulation

(A and B) Schematics of chronic preparation: a sagittal cross-section (A) and a top-view of cranial window with optic-fiber (B).

(C) Experimental setup for awake imaging.

(D) Left: example sagittal section of a blood volume map registered to the Allen Mouse Brain Atlas (thin gray lines). Right: voxel-to-voxel normalized response to stimulation of the plane shown in the left panel.

(E) Bottom: relative hemodynamic response curves to the stimulation of 3 example voxels in the intermediate SC. Top: mean response of the intermediate SC.

(F) Two example sagittal planes from the activity maps of a single animal.

(G) Left: standardized responses of a selection of 72/264 segmented areas. Mean responses are shown for 3 different mice. Response for each mouse is an average of 6 trials. Right: inactive (gray) and active (red) areas colored based on significance threshold corrected for multiple comparisons ($p < 0.05$).

(H) Mean response of each segmented area shown in (G) during the 2 s after the start of the stimulus for 6 different NTSR mice and the average across all mice. Non-significant areas ($p > 0.05$) are set to 0 in the average.

(I) Projection of the average activity vector from (H) onto a map of the mouse brain.

(J) Average time course of each of the 264 segmented areas for each cell type. Black bars along the bottom indicate span of the labeled brain regions.

The blue lines in (E), (G), and (J) indicate the duration of stimulation.

CTX: cortex, sCTX: cortical subplate, TH: thalamus, HYP: hypothalamus, MB: midbrain, HB: hindbrain, CB: cerebellum, AUD: auditory cortex, MO: motor cortex, RSP: retrosplenial cortex, SS: somatosensory cortex, VIS: visual cortex, AMG: amygdala complex, HIPP: hippocampus, CP: caudoputamen, LS: lateral septum, AT: anterior thalamus, LGN: lateral geniculate nucleus, VMT: ventromedial thalamus, VP: ventral posterior thalamus, LHA: lateral hypothalamic area, PH: posterior hypothalamic area, ZI: zona incerta, MLR: mesencephalic locomotor region, CS: superior central nucleus raphe, GRN: gigantocellular reticular nucleus, PG: pontine gray, PRN: pontine reticular nuclei, CENT: cerebellar lobuli, FL: flocculus.

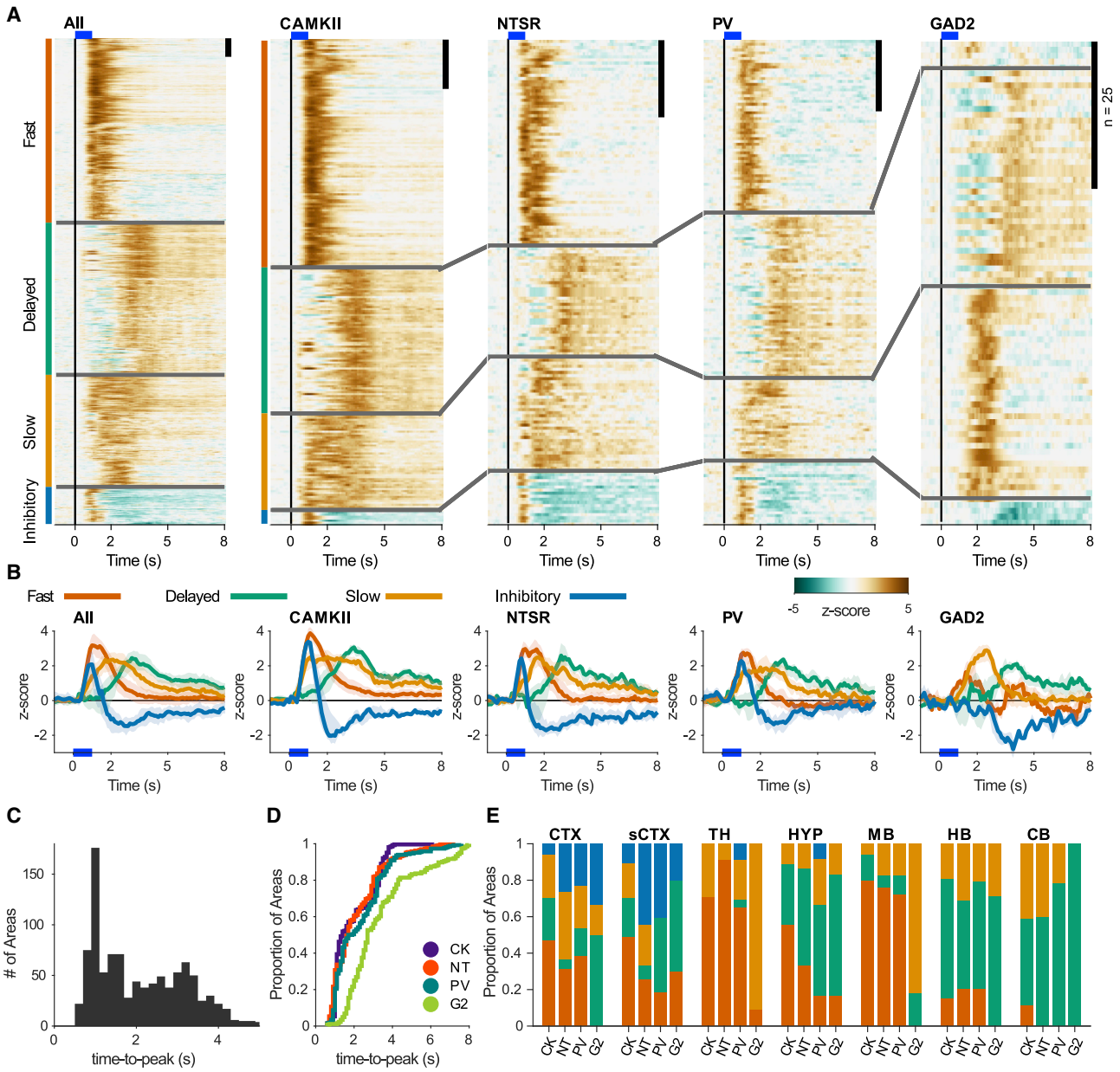

Figure 3. Distribution of temporal response dynamics

(A) Normalized responses to optic stimulation, organized into their respective clusters: fast (orange), delayed (green), slow (yellow), and inhibitory (blue). The black scale bar at the top right of each panel represents 25 areas. The blue line represents the 1 s optical stimulus. Left panel: responses of all areas that had a statistically significant response across all cell populations (n = 659). The other panels are the active areas in each mouse line (CK = 246, NT = 157, PV = 170, G2 = 82).

(B) Average response of each of the clustered responses. Shaded area corresponds to standard deviation.

(C) Histogram of the time-to-peak of each active area in all mouse lines.

(D) Cumulative histogram of time-to-peak in each mouse line.

(E) Proportion of each response type sorted by brain area and mouse line.

dynamics of the responses observed (Figure 3C), we performed this comparison in two distinct time windows, an early (0–2 s) and a late (3–8 s) phase (Figure 4A). Complete lists and 3-dimensional (3D) visualizations of the responsive areas are provided in Table S2 and Videos S3 and S4.

The distribution of responsive areas across the brain in the early and late phases followed different patterns for each of the cell classes (see Figures 4A and 4C). Stimulating CAMKII, NTSR, and PV cell types at high frequency resulted in more responses during the early phase (CK = 193, NT = 138,

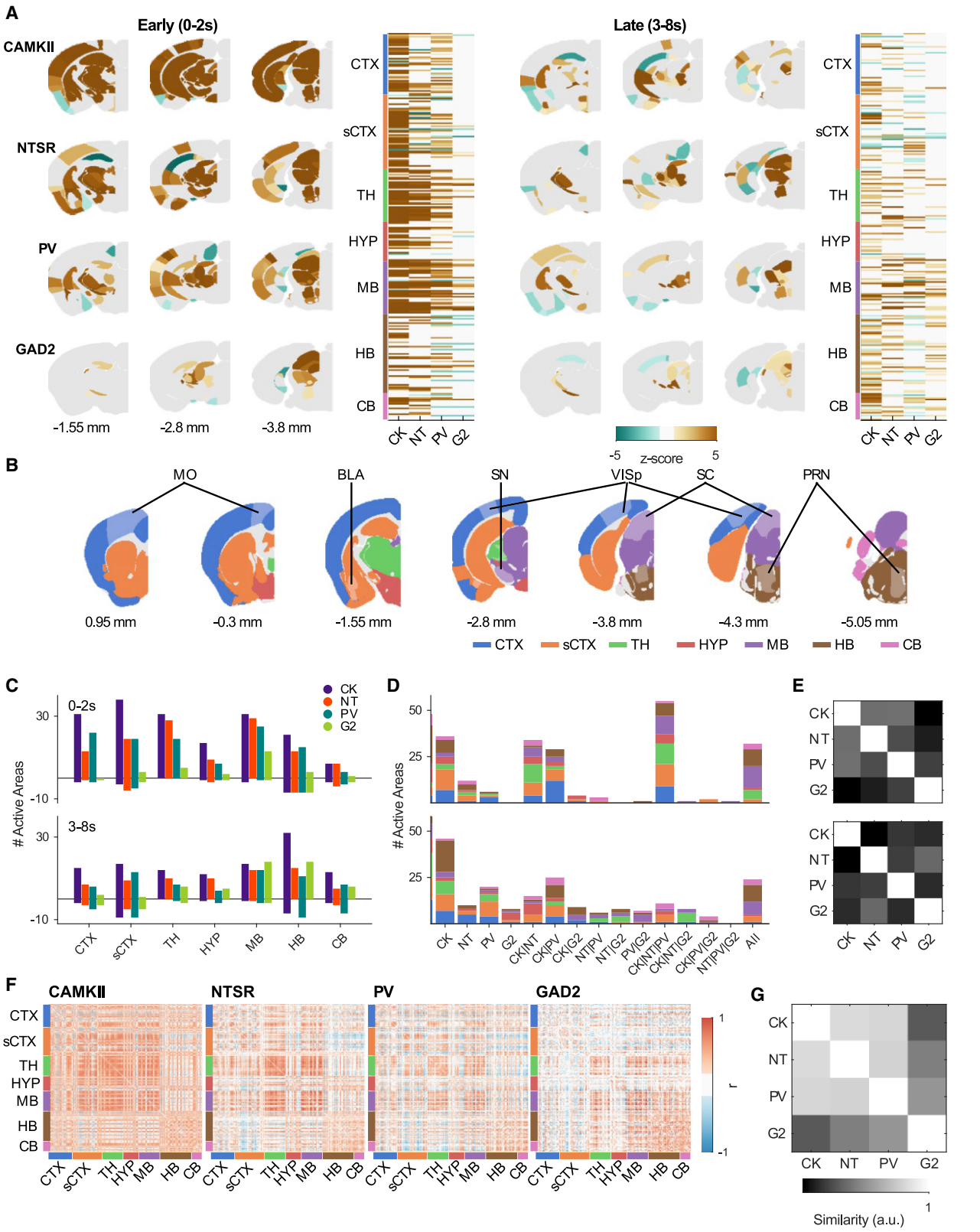

(legend on next page)

PV = 129), as compared to the late phase (CK = 142, NT = 82, PV = 97). In contrast, stimulating GAD2 cells resulted in 41 and 68 areas responding during the early and late phases, respectively. More concretely, the stimulation of CAMKII evoked responses in large portions of the cortex (CTX; 80%, 33/41 areas), cortical subplate (sCTX; 80%, 41/51 areas), thalamus (TH; 80%, 31/36 areas), and midbrain (MB; 89%, 33/37 areas) in the early phase, but was dominated by the hindbrain (HB; 72%, 39/54 areas) and the cerebellum (CB; 79%, 15/19 areas) in the late phase. The NTSR population activated large portions of the MB (78%) and TH (78%) during the early phase (other structures ranged from 34% to 58%) and had less activity but it was more distributed during the late phase (CTX: 24%, sCTX: 27%, TH: 28%, HYP: 38%, MB: 41%, HB: 28%, CB: 42%). PV neurons preferentially modulated the MB (MB: 70%; others: 31%–59%) in the early phase, and the HB (HB: 74%; others: 22%–43%) in the late phase. In GAD2 mice, most areas were activated in the MB in the early phase (MB: 38%; others: 2%–19%). During the late phase, GAD2 activated more areas across the whole brain, particularly in the MB (early/late; 38%/54%), the HB (early/late; 19%/33%), and the CB (early/late; 16%/32%). Low-frequency stimulation did not change the overall distribution of responsive areas in early and late phases of the different cell types (Figures S5A and S5B). However, PV and GAD2 mice had a noticeable decrease in activated areas in both the early (high frequency/low frequency—PV: 129/72; GAD2: 41/14) and late (high frequency/low frequency—PV: 97/73; GAD2: 68/9) phases, and NTSR mice had more responsive areas, which are most noticeable in the HB during the late phase (high frequency/low frequency—HB: 28%/93%).

We next looked at the overlap between the areas modulated by the different cell classes (Figures 4D and 4E). We found that in the early phase, up to 93 areas had shared activity between at least 3 of the neuronal populations, 71 were shared by only 2, and 54 were unique. Consistent with the fact that the CAMKII population overlaps with NTSR neurons, when an area was shared by 2 cell lines, in most cases it was between CAMKII and NTSR (34) mice, but interestingly, also with PV (29), even though the anatomical overlap was only ~5%. During the late phase, the specificity increased and only 47 areas were shared by $\geq$3 cell types. When we compared the maximum activity during the early and late phases between cell lines, we found that during the early phase, the greatest similarity was between PV and NTSR with CAMKII (Figure 4E). During the late phase, GAD2 and NTSR mice showed the highest similarity with each other (Figure 4E, bottom), and all of the other pairings showed very low similarity. Low-frequency stimulation was characterized by a large increase in the number of areas activated by NTSR neurons (Figure S5C), but the similarity patterns between mouse lines were unchanged in both the early and late phases (Figure S5D).

Finally, to compare the activated networks from a holistic point of view, we generated functional connectivity maps of the relationship between areas (Figure 4F). To do this, we calculated the pairwise correlation across all of the active areas of each neuronal population and compared the resulting matrices to each other (Figure 4G). Broadly, CAMKII, NTSR, and PV mice had a high level of correlation between areas of the MB and TH. In GAD2, the highest correlations were found between the MB, the HB, and the CB. Low-frequency stimulation in CAMKII and NTSR mice resulted in strong positive correlations among subcortical structures (TH, hypothalamus [HYP], MB, HB, and CB), while the correlation between subcortical and cortical (CTX and sCTX) structures tended to switch polarity (Figure S5E). The change in frequency did not affect the brain-wide correlations of PV mice, while the correlations for GAD2 became more sparse. These results indicate that each collicular cell type modulates distinct, partially overlapping brain-wide networks.

Defensive and fear-related networks are differentially modulated by each cell class

To understand how the activation of each neuronal population triggers distinct behaviors, we compared the activity patterns of each cell type within a list of 30 areas that have been shown to mediate defensive behaviors (Figure 5A). This comparison showed that each neuronal population activated a different subset of areas or modulated the same areas in a different manner. For example, the posterior medial and paraventricular hypothalamic areas (PMH, PVH) were shared uniquely by cell classes that elicited freezing-like behaviors (CK, NT). In contrast, the cuneiform (CUN) was activated by all of the mouse lines but exhibited different temporal dynamics. The CUN had fast transient responses in CAMKII and NTSR and slower sustained responses in PV and GAD2 mice. There were also cases in which different cell types activated the same areas but in opposite directions. For example, parts of the ventral midline thalamus (RE and Xi) and subthalamic nucleus (STN) had positive responses to CAMKII and NTSR stimulation, but were dominated by negative responses in PV mice. Finally, a few areas were similarly activated by all of the mouse lines, including the dorsal periaqueductal gray (PAGd) and zona incerta (ZI). When we compared the correlated activity across this group of areas (Figure 5B) and the similarity of the traces (Figure 5C) across the different mouse lines, CAMKII

Figure 4. Cell-type-specific activation of downstream pathways of the superior colliculus

(A) Activation maps during early (left, 0–2 s) and late (right, 3–8 s) time windows. Three example coronal slices are shown for each mouse line. Active areas are shown in each plane with the mean *Z* score across mice (CK = 6; NT = 6; PV = 13; G2 = 6). Next to the activation maps is the peak response of all areas active in at least 1 mouse line.

(B) Summary of the extent of the imaging locations with major brain structures delineated and a few regions for orientation marked.

(C) Distribution of active areas during early and late phases.

(D) Quantification of shared areas across mouse lines during early (top) and late (bottom) phases. Areas included in 1 group are excluded from the others.

(E) Similarity matrix (between mouse lines) of maximum activity during early (top) and late (bottom) phases.

(F) Pairwise Pearson correlation coefficients between the mean response traces of the 264 segmented areas during the 8 s after stimulus onset.

(G) Similarity between the correlated hemodynamic responses in (F).

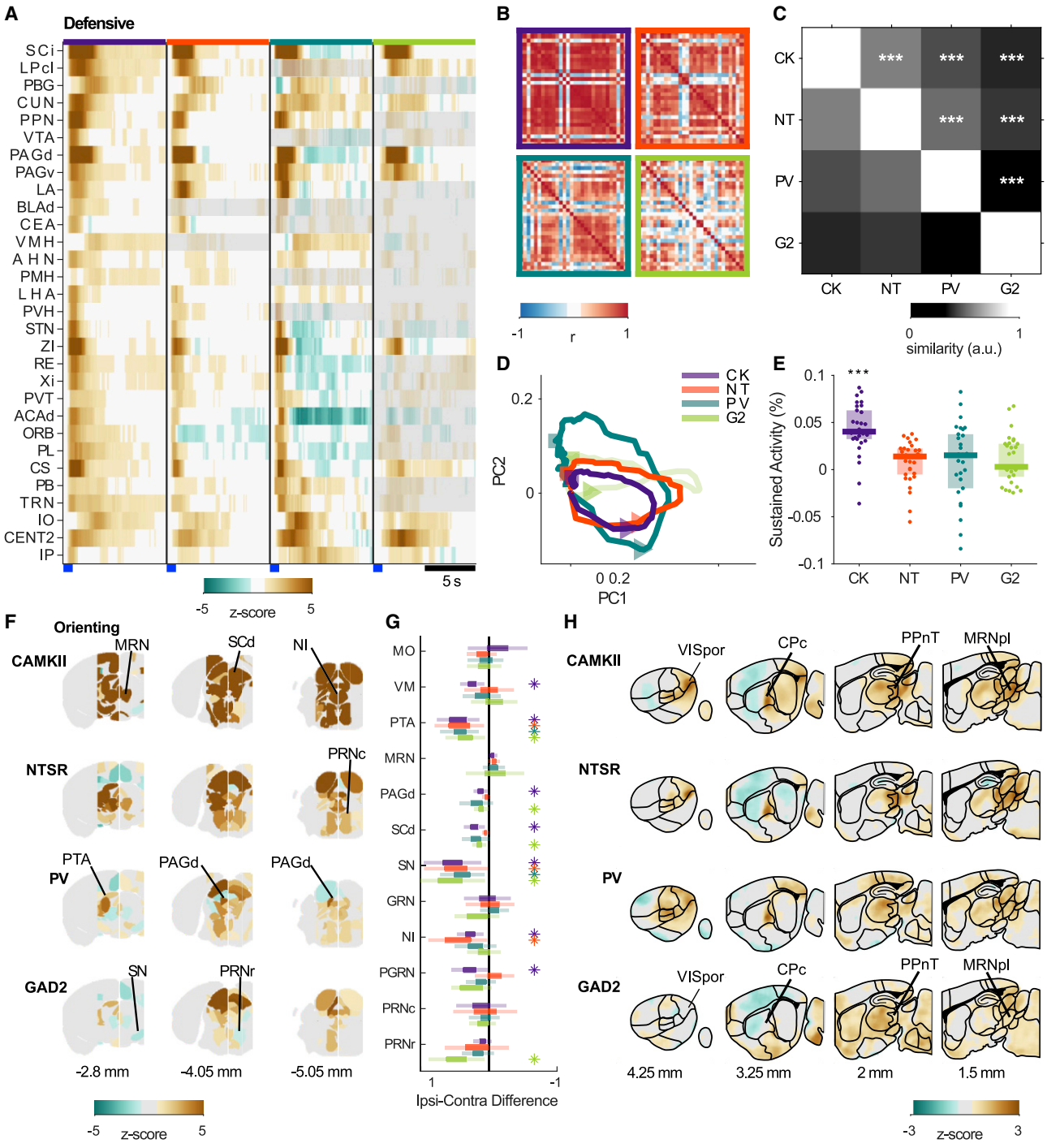

Figure 5. Activity in behaviorally defined networks

(A) Heatmap of the average responses of 30 selected nuclei.

(B) Correlation matrix of the responses in each cell population.

(C) Similarity of the response properties of these 30 areas across cell populations. Statistical difference shown as white asterisks. All comparisons resulted in $p < 10^{-34}$ based on permutation test after Bonferroni correction for multiple comparisons. Comparisons were done using Wilcoxon rank-sum test.

(D) 2D trajectories of the neuronal activity in these 30 brain areas. Triangles and squares represent 1.5 s and 5 s after the stimulus, respectively.

(E) The average sustained activity after 1 s stimulus of each cell type. Each dot represents a brain area.

(F) Comparison of the activity in the nuclei that lie within 2 mm of the midline. Each ipsi-contralateral pair is shown when the difference is the highest within a 4-s window after stimulus onset.

(legend continued on next page)

and NTSR evoked the most similar responses. Visualization of the trajectories followed by the population responses (Figure 5D) showed that CAMKII and NTSR evoked almost identical responses during the first 2 s after the stimulus onset, but then diverged. This was likely due to the more sustained activity evoked by the excitation of CAMKII neurons (Figure 5E).

Activation of the medial part of the SC results in asymmetric activity

Orienting behaviors are thought to be controlled via contralateral projections of the SC (Isa and Sasaki, 2002; Sparks, 2002). In contrast, defensive behaviors are mainly mediated by ipsilateral pathways originating in the medial part of the SC (Dean et al., 1989). We monitored areas on both sides of the brain close to the midline. Consistent with our stimulation of the medial colliculus, we found that each cell line evoked asymmetric activations that were preferentially ipsilateral (Figures 5F and 5G). Activating GAD2 neurons generated the greatest number of asymmetries, including in pontine areas such as the rostral part of the pontine reticular nuclei (PRN), which is in line with the triggered changes in orientation evoked by this cell type (Figure 1).

Novel areas involved in collicular-driven behaviors

Visual inspection of brain-wide activity maps (Figure 5H) revealed a few highly responsive regions that have not previously been studied in the context of collicular-driven behaviors. The four most salient areas were the caudal caudoputamen (CPc); the postrhinal visual area (VISpor); the posterior lateral part of the midbrain reticular formation (MRNpl); and a group of thalamic areas surrounding the medial geniculate complex, the posterior paralaminar nuclei of the thalamus (PPnT) (Herkenham, 1986). The VISpor and CPc are known disynaptic targets of the colliculus but have not been implicated in guiding collicular-driven behaviors (Beltramo and Scanziani, 2019; Bennett et al., 2019; Harting et al., 2001; Takahashi, 1985). The MRNpl and PPnT have not been previously described to receive mono- or disynaptic inputs from retino-recipient neurons of the colliculus.

Correspondence between hemodynamic response and neuronal activity

We found a strong resemblance between the spatial distribution and temporal profile of the hemodynamic response and underlying spiking activity. We used Neuropixels probes to record spiking activity in head-fixed mice evoked by the optogenetic stimulation of NTSR neurons in the SC from a variety of cortical and subcortical brain regions (Figure 6A). A fluorescent dye (DiI) was used to visualize the recording sites and align the probe tracts to the Allen Mouse Brain Atlas and fUSI signal (Figure 6B). While some electrodes showed spiking activity that was triggered by each of the 20 light pulses, others only showed strong spiking responses to the first light pulse (Figure 6C). A raster plot of all 384 recording electrodes for one trial is shown for the penetration from Figure 6B that passed through the cortex, SC, and PAG (Figure 6D). We averaged and normalized fUSI data pooled from 6 previous experiments along the Neuropixels probe tracks and compared them to the spiking activity. In the example recording, we found a high level of correlation between the fUSI and spiking signal ($r = 0.83$; Figure 6E). Across all Neuropixels recordings (4 probe locations, 12 animals, 26 recordings) we found that the spatial activity correlated well with the fUSI signal, with a higher correlation across brain regions where the hemodynamic responses were strong (Figure 6F).

Next, we compared the hemodynamic patterns observed in the fUSI and the local spiking activity in 6 subcortical areas: (1) superficial SC (SCs), (2) deep SC (SCd), (3) PAG, (4) pulvinar (LP), (5) CPc, and (6) PPnT (Figure 5H). In all 6 areas, we found neurons that responded to the optogenetic stimulation of NTSR cells in the SC (Figure 6G). Each area contained neurons that responded to all of the pulses of the 1-s stimulations, cells that responded to only the first stimulation, and others that were inhibited by further pulses. In addition, when accounting for the slow hemodynamic response, we found that the amplitude and the temporal changes in the spiking activity corresponded well to the fUSI signal recorded in the same brain areas (Figures 6G, last column, and S6).

To quantify the neural responses during the 20 optogenetic pulses, we calculated the mean, background-subtracted response of each responding neuron to the 40 ms after each pulse, normalized these 20 measurements to its maximal response, and calculated the area under the curve (AUC). An AUC of 1 indicates a cell that responds equally well to all 20 pulses, whereas negative AUC values indicate more inhibition than excitation. The resulting activity maps sorted by AUC indicate a different distribution of optogenetic responses in the different areas (Figure 6H). We found a higher proportion of sustained responses (high AUC) in the SCs; more transient responses in the PPnT, CPc, and PAG; and a higher percentage of inhibited neurons in the LP (Figure 6I). Subsequently, we classified the responses to optogenetic stimulation measured with Neuropixels probes into the 4 fUSI clusters (fast, delayed, slow, inhibition; Figure 6J). Neurons from the SCs and SCd were mostly found in the early-onset clusters (fast and slow), while delayed responses were more common in the PAG and CPc. The PPnT was dominated by the transient responses found in the fast cluster, and inhibition was most pronounced in the LP. These results show that optogenetic stimulation could be traced from the SC across several synapses. Different response patterns were observed at different stages downstream of NTSR neurons, which correspond well with the differences in the fUSI signal.

Visual responses downstream of NTSR neurons reveal preference for threat stimuli

NTSR neurons respond well to visual stimuli mimicking flying predators that induce aversive behaviors (De Franceschi et al.,

(G) The percentage of difference in the fUSI signal between the ipsi- and contralateral brain areas. The asterisk represents differences that were statistically significant ($p < 0.05$ permutation test, after correction for multiple comparisons). Light-colored lines represent the estimated 95% confidence intervals. Dark portions represent the interquartile range.

(H) Average pixel maps of 4 sagittal sections from each neuronal population that highlight brain areas not commonly reported to mediate collicular-driven behaviors.

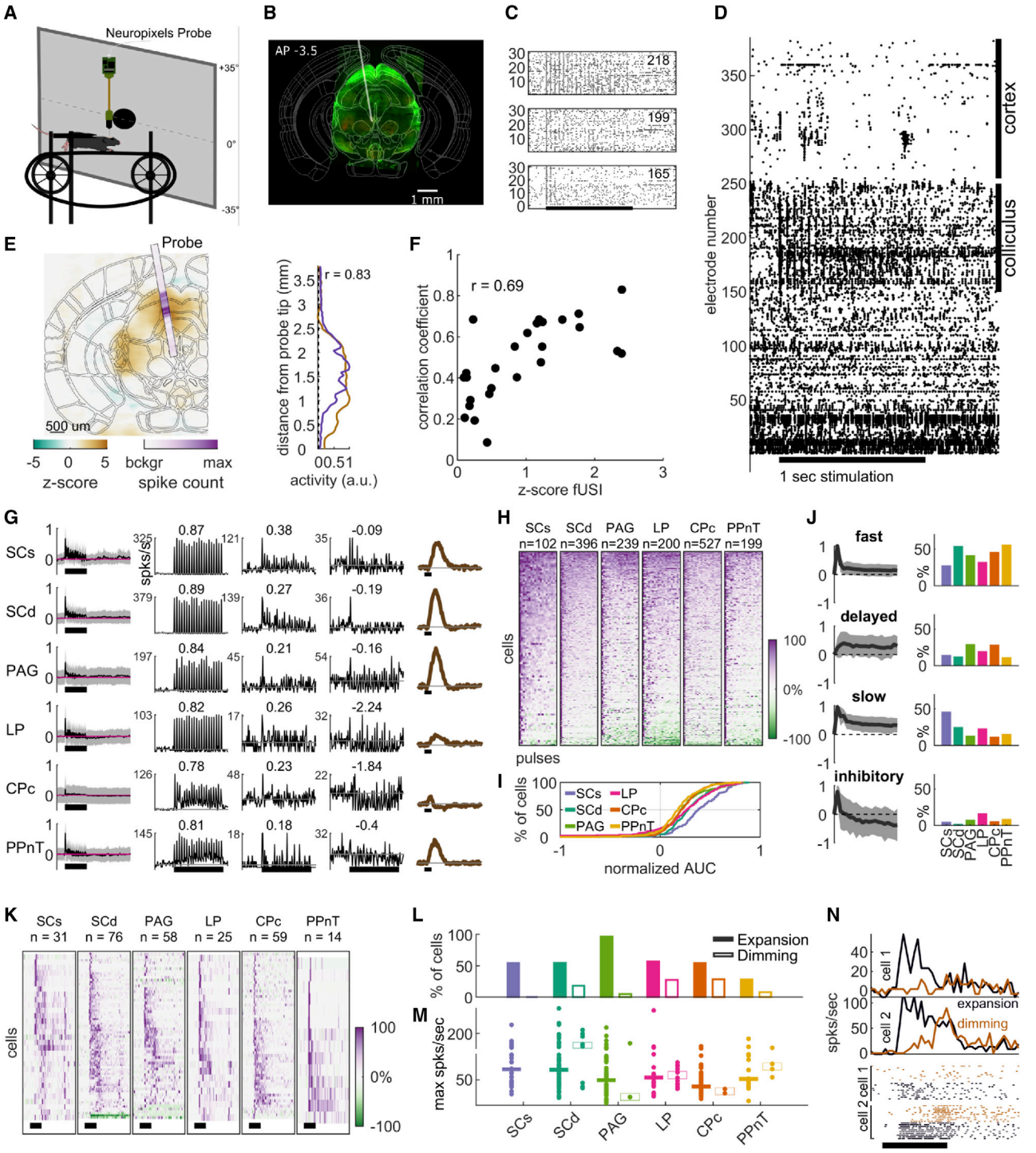

Figure 6. Correspondence of fUSI and spiking activity

(A) Setup for Neuropixels recordings in awake, head-fixed mice.

(B) Example of histological section with NTSR-ChR2^{+} neurons (green) and the probe location indicated with a gray line.

(C) Raster of spikes for 30 repetitions of the optogenetic stimulus for 3 example electrodes. Black bar = stimulus time (1 s, 20 pulses).

(D) Raw spiking data of the probe shown in (B) during a 1-s stimulation of NTSR neurons.

(E) Overlay of fUSI and spiking activity for a colliculus recording. r = correlation coefficient of the average activity on the probe and the corresponding pixels of the fUSI data.

(legend continued on next page)

2016; Gale and Murphy, 2014; Yilmaz and Meister, 2013). We found different types of responses to looming stimuli in optogenetically activated neurons in all tested brain areas (Figures 6K and S7A). When presented with an ecologically less salient stimulus (dimming circle), we did not detect responses in the neurons of the SCs (Figure 6L). In all areas, fewer neurons responded to dimming stimuli, compared to looming stimuli (Figures 6L–6N). We found similar results when including units that did not respond to optogenetic stimulation (Figure S7B). These data show that ecologically relevant visual information is present throughout the multi-synaptic downstream networks of the colliculus that is revealed during opto-fUSI imaging.

Inhibition of PPnT facilitates habituation to repeated stimulation of NTSR neurons

Finally, we investigated the role of the PPnT in collicular-driven behaviors. We chemogenetically suppressed activity of its neurons while optogenetically stimulating NTSR neurons in the SC. We injected an AAV coding for the inhibitory designer receptor exclusively activated by designer drugs (DREADD) hM4D(Gi) into the PPnT of Ntsr x ChR2 mice (Figures 7A and 7B). Mice were tested in the open field arena (Figure 1A) and used 1 s 20 Hz optogenetic stimulations in 5 experimental sessions (Figure 7A). To inhibit the PPnT, clozapine N-oxide (CNO) was injected intraperitoneally 30–40 min before the beginning of the second session.

We found that the inhibition of PPnT increased the variability in the responsiveness of mice to the optical stimulation (Figures 7C–7E). This variability manifested as an increased speed (Figure 7G, session 2, Mann-Whitney *U* test; $p = 0.013$) and a decrease in the probability that arrest would be triggered (Figure 7H, session 2, Mann-Whitney *U* test; $p = 0.008$; Video S5). An examination of the evolution of behavior over trials within session 2 (CNO) revealed that hM4D(Gi) mice habituated more rapidly to the stimulus (Figure 7F). During subsequent sessions, mice did not regain the lost behavioral response (Figure 7G) and tended to maintain a higher speed than controls during the stimulation periods (Figure 7H).

We then investigated the relationship between stopping behavior and the location of hM4D(Gi) expression in the PPnT. No correlations were found along the AP, ML, DV axes, or the extent of the expression (Figures S8A–S8D; Pearson coefficient $r = 0.112$, 0.245, −0.293, and −0.297, respectively). Regarding the DREADD expression in the different areas included in the PPnT and caudal LP, all of the mice had expression in the posterior limiting nucleus of the thalamus (POL). Expression in other areas did not decrease the stopping probability (Figures S8E and S8F). Overall, these results suggest that the inhibition of the PPnT, most likely through the POL, facilitates habituation to the repeated activation of collicular NTSR neurons.

DISCUSSION

In this study, we combined fUSI with optogenetics to reveal the whole-brain neuronal networks that link individual cell types of the SC with a triggered behavior. Our results support the notion that in the SC individual cell types trigger behaviors, not via single dedicated pathways, but instead via distinct brain-wide networks that share a common set of nodes (Figure 8). This highlights the potential of opto-fUSI as a tool for uncovering the different brain-wide networks linked with different behaviors.

Collicular cell types activate different, partially overlapping downstream networks

A variety of previous lines of evidence are consistent with our finding that the activation of different cell types of the SC leads to the broad yet restricted propagation of information across the brain. We found that each collicular cell type relayed information through a different downstream network that converges in a few key nodes (Figures 4 and 5). Our fUSI experiments show that the activation of each cell type modulated the neural activity of at least 82 and up to 246 brain areas. Among the pathways activated were a set of areas that are consistent with known output pathways of the SC and that have been identified to trigger freezing and escape behaviors (Evans et al., 2018; Gale and Murphy, 2014, 2018; Shang et al., 2015, 2018; Zhang et al., 2019). Here, we demonstrate that the activation of the same neural populations results in neural activity in a much larger than expected set of downstream areas. This extensive dissemination of information is likely due in part to recurrent connectivity within the SC (Gale and Murphy, 2018; Whyland et al., 2020), as well as recurrent feedback connections that include the ZI, substantia nigra, and PBG (Bolton et al., 2015; May, 2006; Redgrave et al., 2010; Wolf et al., 2015). While we do observe the previously

(F) Dependence of correlation between fUSI and probe recordings on overall fUSI response strength. Each data point corresponds to 1 probe recording in the colliculus, thalamus, or striatum. The *Z* score comes from the averaged fUSI *Z* score NTSR brain map.
(G) Average response (averaged across all optogenetic stimuli, background-subtracted, and normalized) of sorted units in 6 selected areas (left; means ± SDs). Responses to optogenetic stimulation of 3 example cells for each area. The cell with the highest area under the curve (AUC) (second column), the medium AUC (third column), and the lowest AUC (fourth column), as well as the temporal fUSI response (last column). Numbers indicate AUCs.
(H) Response strength to each optogenetic pulse sorted by AUC. 0% is background activity. N indicates the number of single units.
(I) Cumulative distribution of AUCs for each area.
(J) Responses to the stimulation were classified into the 4 fUSI classes. Average and SD of the normalized response strength for each class as well as average response strength for each class (average AUC for fast: 0.22, delayed: 0.29, slow: 0.42, inhibitory: −0.16). Percentage of cells for each response type and area (right).
(K) Normalized responses to a black looming disk of all optogenetically activated cells with looming responses in each area. N indicates the number of responding cells.
(L) Percentage of optogenetically activated cells with looming or dimming responses. 100% for looming/dimming for SCs n = 57/6, SCd n = 139/44, PAG n = 60/59, LP n = 44/44, CPc n = 109/7, PPnT n = 50/50.
(M) Maximal response strength to expansion and dimming stimuli for each responding cell and their median per area.
(N) Example of a cell with looming, but without dimming response (cell 1), and a cell responding to both (cell 2).

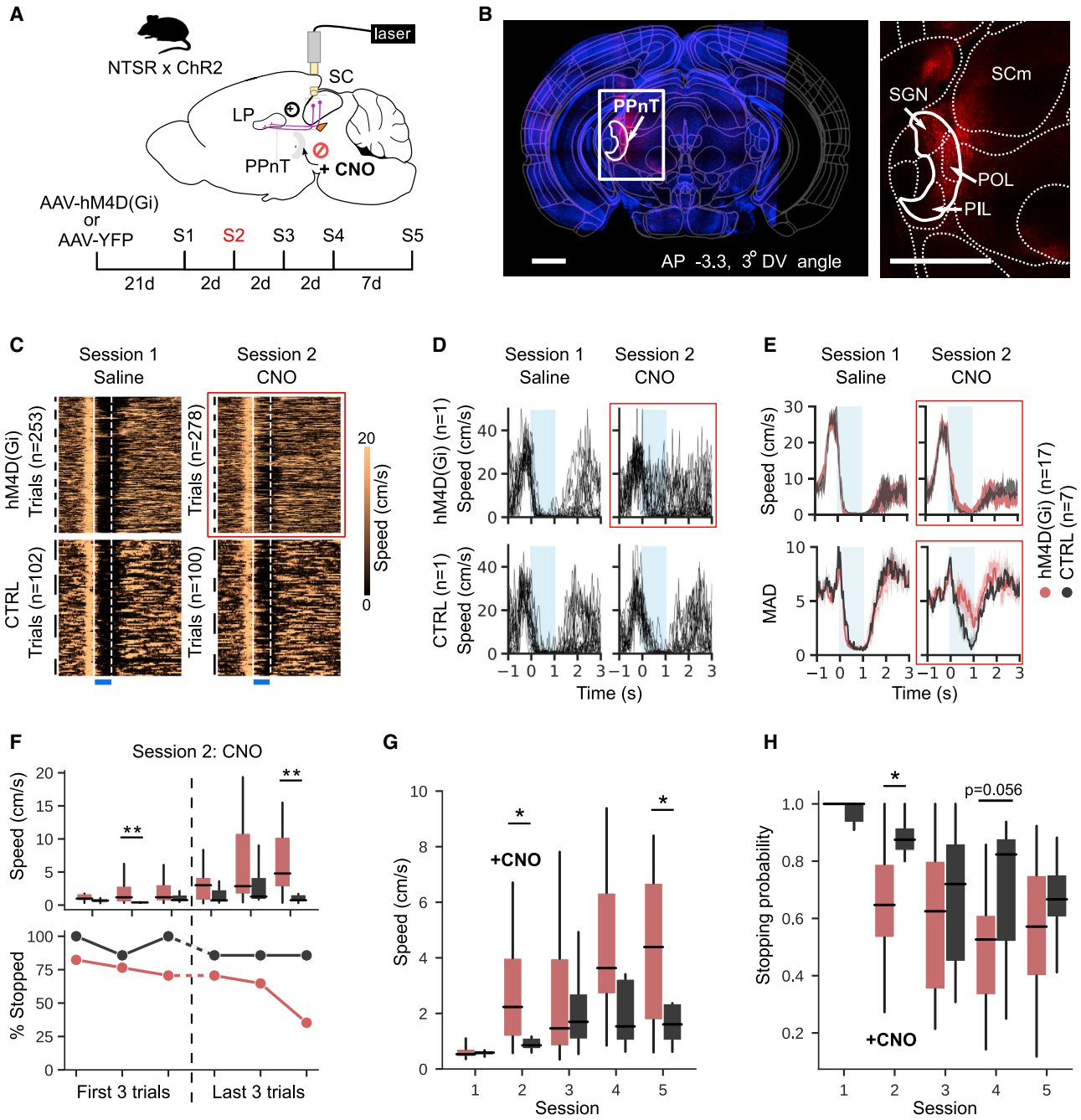

Figure 7. PPnT inhibition facilitates habituation to repeated optogenetic stimulation

(A) Experimental paradigm.

(B) Expression of hM4D(Gi) (red) in the PPnT. Left, coronal section aligned to Allen Mouse Brain Atlas. White rectangle indicates injection site and corresponds to right, zoomed in area. Scale bar, 1 mm.

(C) Speed traces of mice expressing hM4D(Gi) (top row, n = 17) and controls (n = 7, bottom row), expressing yellow fluorescent protein (YFP). Black lines delineate trials belonging to single animals. White lines delineate onset and offset of optogenetic stimulus.

(D) Speed traces from all trials in session 1 (left) and 2 (right) from 1 example animal from each group.

(E) Top row: median speed traces from all hM4D(Gi) (red) and control (CTRL) (gray) mice. Bottom row: mean absolute deviation of the speed for hM4D (red) and CTRL (gray) mice.

(F) Median speed (top row) and stopping probability (bottom row) during the 1-s stimulation of hM4D(Gi) (red) and CTRL (gray) mice, during session 2.

(legend continued on next page)

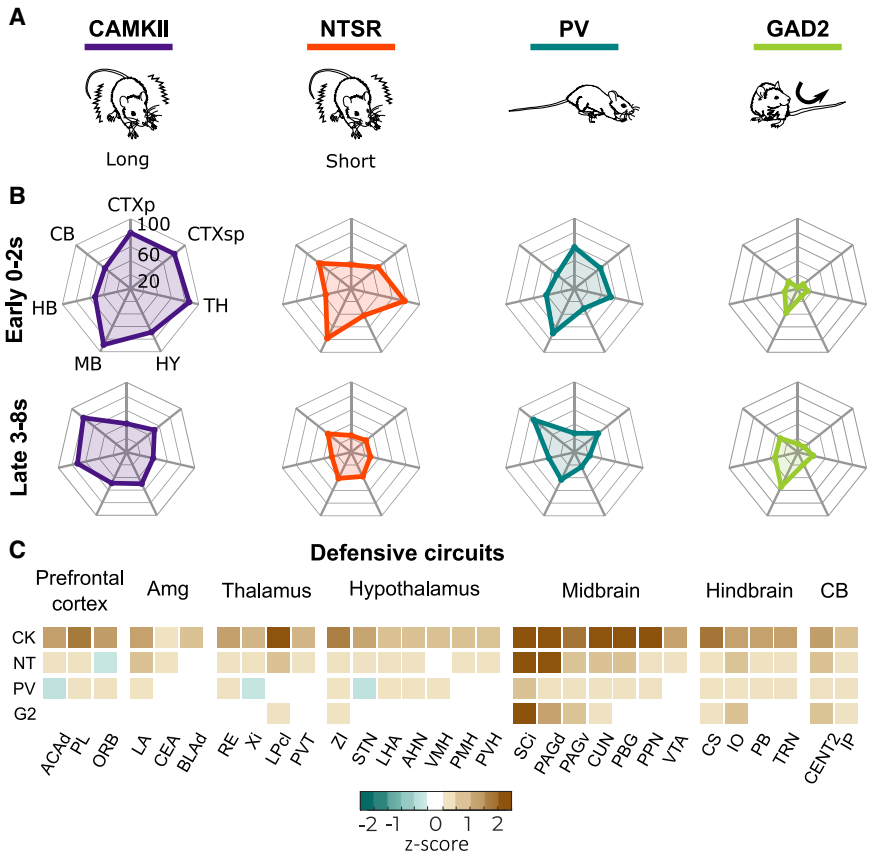

Figure 8. Summary

(A) Optogenetic activation of different collicular cell types evokes distinct behaviors and activates different brain-wide networks.

(B) Percentage of activated areas across major brain structures. The effects are shown for early (0–2 s from stimulus onset, top row), and late (3–8 s from stimulus onset, bottom row) time windows.

(C) Heatmap depicting the effect of activating different collicular cell types in a selected set of areas previously shown to be involved in defensive behaviors. The color indicates the mean normalized response (*Z* score) during the 8 s after stimulus onset. White spaces indicate areas that did not have statistically significant changes.

reported nuclei, brain-wide fUSI allowed us to observe functional networks downstream of cell types in the SC across most of the brain.

Conversely, the brain-wide activity we observed shows a higher degree of specificity than we would predict from mesoscale maps of area-to-area connectivity (Oh et al., 2014). If, for example, we assume that each brain area, such as the retinal recipient layers of the SC, projects to at least 6 downstream structures, we need only 3 synapses to modulate 216 brain areas. In many cases, this underestimates the number of projections that a brain area makes. The retina sends projections to ~40 targets (Martersteck et al., 2017), while the primary visual cortex innervates at least 18 cortical and subcortical areas (Han et al., 2018). We saw our maximal spread of activity when stimulating CAMKII neurons, which modulated 246 areas across the early and late phases, while NTSR neurons modulated 157 areas. This restriction in the extent of dissemination is likely due to the cell-type-specific connections made in the SC and other brain regions. In the SC, distinct output pathways are known to selectively sample retinal inputs and project to selected downstream areas (Gale and Murphy, 2014; Reinhard et al., 2019). In addition, outputs of the SC to the LP have been shown to be relayed to a narrow set of targets (Beltramo and Scanziani, 2019; Wei et al., 2015). This cell-type-specific relay of information is a common feature of several investigated brain structures, including the visual cortex, amygdala, and ventral tegmental area (VTA) (Beier et al., 2019; Fadok et al., 2017; Han et al., 2018).

Optogenetically triggered behavior is consistent with the network activity

How the SC routes the cell-type-specific information to evoke different behaviors corresponded well with the observed similarities and differences in the network activity. We found that the activation of CAMKII and NTSR neurons resulted in an interruption of locomotor activity, which was likely the result of the high overlap between these two populations (Figure S1A) and was reflected in the similarity in the brain-wide activity evoked by each population (Figure 4). In addition, we showed that PV and GAD2 neurons had minimal overlap with the other studied populations (Figures S1B–S1D). Their activation facilitated different behaviors, orienting movements, which was consistent with the increases in the activity observed in motor areas of the cerebellum and hindbrain.

Three brain areas that exemplify how different behaviors could be mediated by different collicular cell types include the STN, the CUN, and midline thalamus nuclei. First, activating CAMKII or NTSR neurons resulted in an increase in activity of the STN, a region involved in the interruption of behavior (Aron and Poldrack, 2006; Fife et al., 2017). In contrast, the activity of the STN was suppressed or not detectable after the stimulation of PV and GAD2, where locomotion was not interrupted. This suggests that the STN is either activated to pause ongoing behaviors or silenced to promote escape strategies. Second, we found distinct temporal responses in the CUN across mouse lines.

(G) Median speed of hM4D(Gi) (red) and CTRL (gray) mice, during the 1-s stimulations across sessions.

(H) Stopping probability of hM4D(Gi) (red) and CTRL (gray) mice, during the 1-s stimulations across sessions. Boxplots indicate median, interquartile range, and 5th to 95th percentiles of the distribution.

Statistical analysis used Mann-Whitney *U* test. *p < 0.05; **p < 0.01.

The CUN has been shown to trigger freezing and escape (Dean et al., 1989), participate in locomotion (Capelli et al., 2017; Mori et al., 1989), and modulate cardiovascular activity (Korte et al., 1992). We observed transient responses in animals with freezing-like behaviors (CAMKII, NTSR) and slow sustained responses in animals with continuous locomotion (PV, GAD2). It is plausible that different neuronal subpopulations of the CUN are functionally connected with different collicular cell types to play various roles in behaviors. Third, we show that the nuclei of the ventral midline thalamus (RE and Xi), which play a role in decision making when exposed to threat (Salay et al., 2018), are modulated by both PV and CAMKII neurons but in opposite directions, with sustained activation and inhibition, respectively (Figure 5). Our results suggest that opto-fUSI is a reliable method for studying how the cell-type-specific information is disseminated from the SC across the brain to trigger behavior.

Opto-fUSI reveals new players in aversive behavior driven by the SC

In our experiments, we observed areas consistently activated that have not previously been reported to be involved in mediating visually guided aversive behaviors. Precise circuit dissections have highlighted three major pathways that pass information about visual threat from the SC to downstream areas. These cell-type-specific pathways include projections to the amygdala through the LP or the PBG (Shang et al., 2015, 2018; Wei et al., 2015) and projections to the PAGd (Evans et al., 2018). These dissections have led to an atomistic understanding of how the SC mediates aversive behaviors. Here, we observed activity in many areas across the brain and four of them captured our attention: the caudal part of the CPc, the VISpor, the MRNpl, and the PPnT. Some of these areas have been implicated in modulating visual behavior (Nagy et al., 2003; Reig and Silberberg, 2014; Schulz et al., 2009; Wilson et al., 1983). In particular, the PPnT was reliably activated upon both optogenetic stimulation of NTSR neurons in the SC and during the presentation of visual stimuli (Figures 5 and 6). The PPnT is known for its role in associative learning during auditory fear conditioning and mediating fear discrimination and extinction (Gross and Canteras, 2012; Grosso et al., 2018). Our experiments revealed that this group of areas plays a similar role in behaviors triggered by the SC by acting to suppress habituation. Our results are consistent with the proposed role of PPnT in fear extinction and suggest that PPnT is part of the pathway downstream of the SC modulating innate behaviors.

Optogenetics and the relationship between fUSI, neural activity, and behavioral outcomes

One of the key questions for fUSI imaging is the degree to which it faithfully represents the underlying neural activity, and in consequence how it could be used to study behavior. In the context of fMRI, while it is generally accepted that the measured blood oxygen-level-dependent (BOLD) signal changes are associated with neuronal activity (Logothetis and Wandell, 2004), how and where the BOLD signal reliably represents the spiking activity of individual neurons remains an open question (Ekstrom, 2010). Like fMRI, fUSI relies on the indirect measurement of neural activity through hemodynamic changes, in this case, in cerebral blood volume. Recently, it has been shown that fUSI signals can reliably represent both increases and decreases in local neuronal activity (Aydin et al., 2020; Macé et al., 2018; Nunez-Elizalde et al., 2021). We provide additional evidence that the changes in blood volume detected by fUSI are consistent with the local changes in neuronal activity in several different brain regions, including parts of the cortex, striatum, hippocampus, thalamus, and midbrain (Figures 6 and S6).

Of note, optogenetic stimulation has been shown to be able to evoke frequency-dependent behavioral outcomes (Barbano et al., 2016; Viskaitis et al., 2017; Weitz et al., 2015), and it is therefore likely that the spread of the neural activity is subject to the patterns that drive them. However, in our experiments, we tested high- (20–50 Hz) and low- (5 Hz) frequency stimulations and found both the behavioral and neural circuits activated to be largely conserved. Even so, it is important to note that optogenetic stimulations alone, which generate synchronous activation, cannot tell us how natural stimuli would drive the activity of a specific cell type and its downstream pathways to generate a particular behavior. For example, visual stimuli are routed through different cortical and subcortical pathways and we cannot predict how the interactions between them would affect the overall outcome. Our results only capture one behavioral effect of the causal influence of the cell types tested and will miss the interactions between the different streams of information. Nonetheless, our results provide insights into how individual streams disseminate information across the brain; by selecting a single cell type of the colliculus, we capture the brain-wide functional connectivity and the behavioral consequence of its activation. This allows us to observe one of the behaviors to which each of these cell types contributes and through which putative pathways this is mediated and regulated.

In conclusion, we showed that the neural pathways involved in mediating and modulating collicular-driven behaviors are far more complex than previously reported. We demonstrate how combining fUSI with targeted cell type manipulations and natural stimuli will allow us to understand how different brain regions act in concert to guide defensive behaviors under a variety of conditions.

STAR★METHODS

Detailed methods are provided in the online version of this paper and include the following:

- KEY RESOURCES TABLE
- RESOURCE AVAILABILITY
  - Lead contact
  - Materials availability
  - Data and code availability
- EXPERIMENTAL MODEL AND SUBJECT DETAILS
  - Animals
- METHOD DETAILS
  - General surgical procedures
  - Viral injections
  - Cranial windows and optic-fiber implantations
  - Behavioral tests
  - Protocol of functional ultrasound imaging

- Generation of a functional ultrasound image
- Electrophysiological recordings
- Visual stimuli
- Immunohistochemistry

- QUANTIFICATION AND STATISTICAL ANALYSIS
  - Analysis of behavioral data
  - Analysis of fUSI data
  - Analysis of neuropixels recordings

SUPPLEMENTAL INFORMATION

Supplemental information can be found online at https://doi.org/10.1016/j.neuron.2021.04.008.

ACKNOWLEDGMENTS

This work was supported by the FWO (G094616N to K.F., G091719N to K.F. and A.U., MEDI-RESCU2-AKUL/17/049 and 1197818N to A.U., 1197818N/1197820N to A.S.-D., 11C5119N/11C5121N to A.C., and 12S7920N to K.R.); The Leducq Foundation (15CVD02 to A.U.); the European Union's Horizon 2020 research and innovation program under the Marie Skłodowska-Curie grant agreement no. 665501 (12S7917N to K.R.); A Master Mind Scholarship (F200075 to D.L.); and the imec PhD fellowship to T.L.. Also, we would like to thank Adrien Philippon and Dries Kil for their technical support, Yun-An Huang for help in the fUSI analysis, and Micheline Grillet and Clement Brunner for helping us to develop the opto-fUSI preparation.

AUTHOR CONTRIBUTIONS

Conceptualization, A.S.-D., A.C., G.M., A.U., and K.F.; experimental setup and development, A.S.-D., K.R., T.L., G.M., A.U., and K.F.; experiments, A.S.-D., A.C., K.R., and D.L.; analysis, A.S.-D., A.C., K.R., B.N., D.L., and K.F.; software, G.M. and A.U.; writing & editing, A.S.-D., A.C., K.R., B.N., G.M., A.U., and K.F.

DECLARATION OF INTERESTS

A.U. is the founder and a shareholder of AUTC, commercializing neuroimaging solutions for preclinical and clinical research.

Received: August 26, 2020
Revised: March 1, 2021
Accepted: April 10, 2021
Published: April 29, 2021

REFERENCES

Ahrens, M.B., Li, J.M., Orger, M.B., Robson, D.N., Schier, A.F., Engert, F., and Portugues, R. (2012). Brain-wide neuronal dynamics during motor adaptation in zebrafish. Nature *485*, 471–477.

Aimon, S., Katsuki, T., Jia, T., Grosenick, L., Broxton, M., Deisseroth, K., Sejnowski, T.J., and Greenspan, R.J. (2019). Fast near-whole-brain imaging in adult Drosophila during responses to stimuli and behavior. PLoS Biol. *17*, e2006732.

Aron, A.R., and Poldrack, R.A. (2006). Cortical and subcortical contributions to Stop signal response inhibition: role of the subthalamic nucleus. J. Neurosci. *26*, 2424–2433.

Aydin, A.-K., Haselden, W.D., Goulam Houssen, Y., Pouzat, C., Rungta, R.L., Demené, C., Tanter, M., Drew, P.J., Charpak, S., and Boido, D. (2020). Transfer functions linking neural calcium to single voxel functional ultrasound signal. Nat. Commun. *11*, 2954.

Babcock, D.S., Patriquin, H., LaFortune, M., and Dauzat, M. (1996). Power doppler sonography: basic principles and clinical applications in children. Pediatr. Radiol. *26*, 109–115.

Baden, T., Berens, P., Franke, K., Román Rosón, M., Bethge, M., and Euler, T. (2016). The functional diversity of retinal ganglion cells in the mouse. Nature *529*, 345–350.

Barbano, M.F., Wang, H.L., Morales, M., and Wise, R.A. (2016). Feeding and reward are differentially induced by activating GABAergic lateral hypothalamic projections to VTA. J. Neurosci. *36*, 2975–2985.

Beier, K.T., Gao, X.J., Xie, S., DeLoach, K.E., Malenka, R.C., and Luo, L. (2019). Topological Organization of Ventral Tegmental Area Connectivity Revealed by Viral-Genetic Dissection of Input-Output Relations. Cell Rep. *26*, 159–167.e6.

Beltramo, R., and Scanziani, M. (2019). A collicular visual cortex: neocortical space for an ancient midbrain visual structure. Science *363*, 64–69.

Benjamini, Y., and Hochberg, Y. (1995). Controlling the False Discovery Rate: A Practical and Powerful Approach to Multiple Testing. J. R. Stat. Soc. B *57*, 289–300.

Bennett, C., Gale, S.D., Garrett, M.E., Newton, M.L., Callaway, E.M., Murphy, G.J., and Olsen, S.R. (2019). Higher-Order Thalamic Circuits Channel Parallel Streams of Visual Information in Mice. Neuron *102*, 477–492.e5.

Bernal-Casas, D., Lee, H.J., Weitz, A.J., and Lee, J.H. (2017). Studying Brain Circuit Function with Dynamic Causal Modeling for Optogenetic fMRI. Neuron *93*, 522–532.e5.

Bolton, A.D., Murata, Y., Kirchner, R., Kim, S.Y., Young, A., Dang, T., Yanagawa, Y., and Constantine-Paton, M. (2015). A Diencephalic Dopamine Source Provides Input to the Superior Colliculus, where D1 and D2 Receptors Segregate to Distinct Functional Zones. Cell Rep. *13*, 1003–1015.

Brainard, D.H. (1997). The Psychophysics Toolbox. Spat. Vis. *10*, 433–436.

Brunner, C., Grillet, M., Sans-Dublanc, A., Farrow, K., Lambert, T., Macé, E., Montaldo, G., and Urban, A. (2020). A Platform for Brain-wide Volumetric Functional Ultrasound Imaging and Analysis of Circuit Dynamics in Awake Mice. Neuron *108*, 861–875.e7.

Capelli, P., Pivetta, C., Soledad Esposito, M., and Arber, S. (2017). Locomotor speed control circuits in the caudal brainstem. Nature *551*, 373–377.

Cuntz, H., Forstner, F., Borst, A., and Häusser, M. (2010). One rule to grow them all: A general theory of neuronal branching and its practical application. PLoS Comput. Biol. *6*, e1000877.

Davies, D.L., and Bouldin, D.W. (1979). A Cluster Separation Measure. IEEE Trans. Pattern Anal. Mach. Intell. *1*, 224–227.

De Franceschi, G., Vivattanasarn, T., Saleem, A.B., and Solomon, S.G. (2016). Vision Guides Selection of Freeze or Flight Defense Strategies in Mice. Curr. Biol. *26*, 2150–2154.

Dean, P., Redgrave, P., and Westby, G.W.M. (1989). Event or emergency? Two response systems in the mammalian superior colliculus. Trends Neurosci. *12*, 137–147.

Ekstrom, A. (2010). How and when the fMRI BOLD signal relates to underlying neural activity: the danger in dissociation. Brain Res. Brain Res. Rev. *62*, 233–244.

Evans, D.A., Stempel, A.V., Vale, R., Ruehle, S., Lefler, Y., and Branco, T. (2018). A synaptic threshold mechanism for computing escape decisions. Nature *558*, 590–594.

Fadok, J.P., Krabbe, S., Markovic, M., Courtin, J., Xu, C., Massi, L., Botta, P., Bylund, K., Müller, C., Kovacevic, A., et al. (2017). A competitive inhibitory circuit for selection of active and passive fear responses. Nature *542*, 96–100.

Fife, K.H., Gutierrez-Reed, N.A., Zell, V., Bailly, J., Lewis, C.M., Aron, A.R., and Hnasko, T.S. (2017). Causal role for the subthalamic nucleus in interrupting behavior. eLife *6*, 1–13.

Friston, K.J., Holmes, A.P., Poline, J.B., Grasby, P.J., Williams, S.C., Frackowiak, R.S., and Turner, R. (1995). Analysis of fMRI time-series revisited. Neuroimage *2*, 45–53.

Gale, S.D., and Murphy, G.J. (2014). Distinct representation and distribution of visual information by specific cell types in mouse superficial superior colliculus. J. Neurosci. *34*, 13458–13471.

Gale, S.D., and Murphy, G.J. (2016). Active Dendritic Properties and Local Inhibitory Input Enable Selectivity for Object Motion in Mouse Superior Colliculus Neurons. J. Neurosci. *36*, 9111–9123.

Gale, S.D., and Murphy, G.J. (2018). Distinct cell types in the superficial superior colliculus project to the dorsal lateral geniculate and lateral posterior thalamic nuclei. J. Neurophysiol. *120*, 1286–1292.

Gerfen, C.R., Paletzki, R., and Heintz, N. (2013). GENSAT BAC cre-recombinase driver lines to study the functional organization of cerebral cortical and basal ganglia circuits. Neuron *80*, 1368–1383.

Gross, C.T., and Canteras, N.S. (2012). The many paths to fear. Nat. Rev. Neurosci. *13*, 651–658.

Grosso, A., Santoni, G., Manassero, E., Renna, A., and Sacchetti, B. (2018). A neuronal basis for fear discrimination in the lateral amygdala. Nat. Commun. *9*, 1214.

Han, Y., Kebschull, J.M., Campbell, R.A.A., Cowan, D., Imhof, F., Zador, A.M., and Mrsic-Flogel, T.D. (2018). The logic of single-cell projections from visual cortex. Nature *556*, 51–56.

Harting, J.K., Updyke, B.V., and Van Lieshout, D.P. (2001). Striatal projections from the cat visual thalamus. Eur. J. Neurosci. *14*, 893–896.

Herkenham, M. (1986). New Perspectives on the Organization and Evolution of Nonspecific Thalamocortical Projections (Springer), pp. 403–445.

Hoy, J.L., Bishop, H.I., and Niell, C.M. (2019). Defined Cell Types in Superior Colliculus Make Distinct Contributions to Prey Capture Behavior in the Mouse. Curr. Biol. *29*, 4130–4138.e5.

Inayat, S., Barchini, J., Chen, H., Feng, L., Liu, X., and Cang, J. (2015). Neurons in the most superficial lamina of the mouse superior colliculus are highly selective for stimulus direction. J. Neurosci. *35*, 7992–8003.

Isa, T., and Sasaki, S. (2002). Brainstem control of head movements during orienting; organization of the premotor circuits. Prog. Neurobiol. *66*, 205–241.

Jun, J.J., Steinmetz, N.A., Siegle, J.H., Denman, D.J., Bauza, M., Barbarits, B., Lee, A.K., Anastassiou, C.A., Andrei, A., Aydın, Ç., et al. (2017). Fully integrated silicon probes for high-density recording of neural activity. Nature *551*, 232–236.

Korte, S.M., Jaarsma, D., Luiten, P.G.M., and Bohus, B. (1992). Mesencephalic cuneiform nucleus and its ascending and descending projections serve stress-related cardiovascular responses in the rat. J. Auton. Nerv. Syst. *41*, 157–176.

Lee, H.J., Weitz, A.J., Bernal-Casas, D., Duffy, B.A., Choy, M., Kravitz, A.V., Kreitzer, A.C., and Lee, J.H. (2016). Activation of Direct and Indirect Pathway Medium Spiny Neurons Drives Distinct Brain-wide Responses. Neuron *91*, 412–424.

Lein, E.S., Hawrylycz, M.J., Ao, N., Ayres, M., Bensinger, A., Bernard, A., Boe, A.F., Boguski, M.S., Brockway, K.S., Byrnes, E.J., et al. (2007). Genome-wide atlas of gene expression in the adult mouse brain. Nature *445*, 168–176.

Logothetis, N.K., and Wandell, B.A. (2004). Interpreting the BOLD signal. Annu. Rev. Physiol. *66*, 735–769.

Lopes, G., Bonacchi, N., Frazão, J., Neto, J.P., Atallah, B.V., Soares, S., Moreira, L., Matias, S., Itskov, P.M., Correia, P.A., et al. (2015). Bonsai: an event-based framework for processing and controlling data streams. Front. Neuroinform. *9*, 7.

Maaten, L.V.D., and Hinton, G. (2008). Visualizing Data Using t-SNE. Journal of Machine Learning Research *9*, 2579–2605.

Macé, E., Cohen, I., Montaldo, G., Miles, R., Fink, M., and Tanter, M. (2011). In vivo mapping of brain elasticity in small animals using shear wave imaging. IEEE Trans. Med. Imaging *30*, 550–558.

Macé, E., Montaldo, G., Osmanski, B.-F., Cohen, I., Fink, M., and Tanter, M. (2013). Functional ultrasound imaging of the brain: theory and basic principles. IEEE Trans. Ultrason. Ferroelectr. Freq. Control *60*, 492–506.

Macé, É., Montaldo, G., Trenholm, S., Cowan, C., Brignall, A., Urban, A., and Roska, B. (2018). Whole-Brain Functional Ultrasound Imaging Reveals Brain Modules for Visuomotor Integration. Neuron *100*, 1241–1251.e7.

Madisen, L., Zwingman, T.A., Sunkin, S.M., Oh, S.W., Zariwala, H.A., Gu, H., Ng, L.L., Palmiter, R.D., Hawrylycz, M.J., Jones, A.R., et al. (2010). A robust and high-throughput Cre reporting and characterization system for the whole mouse brain. Nat. Neurosci. *13*, 133–140.

Madisen, L., Mao, T., Koch, H., Zhuo, J.M., Berenyi, A., Fujisawa, S., Hsu, Y.-W.A., Garcia, A.J., 3rd, Gu, X., Zanella, S., et al. (2012). A toolbox of Cre-dependent optogenetic transgenic mice for light-induced activation and silencing. Nat. Neurosci. *15*, 793–802.

Martersteck, E.M., Hirokawa, K.E., Evarts, M., Bernard, A., Duan, X., Li, Y., Ng, L., Oh, S.W., Ouellette, B., Royall, J.J., et al. (2017). Diverse Central Projection Patterns of Retinal Ganglion Cells. Cell Rep. *18*, 2058–2072.

Masullo, L., Mariotti, L., Alexandre, N., Freire-Pritchett, P., Boulanger, J., and Tripodi, M. (2019). Genetically Defined Functional Modules for Spatial Orienting in the Mouse Superior Colliculus. Curr. Biol. *29*, 2892–2904.e8.

Mathis, A., Mamidanna, P., Cury, K.M., Abe, T., Murthy, V.N., Mathis, M.W., and Bethge, M. (2018). DeepLabCut: markerless pose estimation of user-defined body parts with deep learning. Nat. Neurosci. *21*, 1281–1289.

May, P.J. (2006). The mammalian superior colliculus: laminar structure and connections. Prog. Brain Res. *151*, 321–378.

Mori, S., Sakamoto, T., Ohta, Y., Takakusaki, K., and Matsuyama, K. (1989). Site-specific postural and locomotor changes evoked in awake, freely moving intact cats by stimulating the brainstem. Brain Res. *505*, 66–74.

Nagy, A., Eördegh, G., Norita, M., and Benedek, G. (2003). Visual receptive field properties of neurons in the caudate nucleus. Eur. J. Neurosci. *18*, 449–452.

Nakamura, Y., Nakamura, Y., Pelosi, A., Djemai, B., Debacker, C., Hervé, D., Girault, J.-A., and Tsurugizawa, T. (2020). fMRI detects bilateral brain network activation following unilateral chemogenetic activation of direct striatal projection neurons. Neuroimage *220*, 117079.

Nunez-Elizalde, A.O., Krumin, M., Reddy, C.B., Montaldo, G., Urban, A., Harris, K.D., and Carandini, M. (2021). Neural basis of functional ultrasound signals. bioRxiv. https://doi.org/10.1101/2021.03.31.437915.

Oh, S.W., Harris, J.A., Ng, L., Winslow, B., Cain, N., Mihalas, S., Wang, Q., Lau, C., Kuan, L., Henry, A.M., et al. (2014). A mesoscale connectome of the mouse brain. Nature *508*, 207–214.

Pelli, D.G. (1997). The VideoToolbox software for visual psychophysics: transforming numbers into movies. Spat. Vis. *10*, 437–442.

Rabut, C., Correia, M., Finel, V., Pezet, S., Pernot, M., Deffieux, T., and Tanter, M. (2019). 4D functional ultrasound imaging of whole-brain activity in rodents. Nat. Methods *16*, 994–997.

Redgrave, P., Coizet, V., Comoli, E., McHaffie, J.G., Leriche, M., Vautrelle, N., Hayes, L.M., and Overton, P. (2010). Interactions between the midbrain superior colliculus and the basal ganglia. Front. Neuroanat. *4*, 132.

Reig, R., and Silberberg, G. (2014). Multisensory integration in the mouse striatum. Neuron *83*, 1200–1212.

Reinhard, K., Li, C., Do, Q., Burke, E.G., Heynderickx, S., and Farrow, K. (2019). A projection specific logic to sampling visual inputs in mouse superior colliculus. eLife *8*, e50697.

Rousseeuw, P.J. (1987). Silhouettes: a graphical aid to the interpretation and validation of cluster analysis. J. Comput. Appl. Math. *20*, 53–65.

Rubin, J.M., Bude, R.O., Carson, P.L., Bree, R.L., and Adler, R.S. (1994). Power Doppler US: a potentially useful alternative to mean frequency-based color Doppler US. Radiology *190*, 853–856.

Salay, L.D., Ishiko, N., and Huberman, A.D. (2018). A midline thalamic circuit determines reactions to visual threat. Nature *557*, 183–189.

Schindelin, J., Arganda-Carreras, I., Frise, E., Kaynig, V., Longair, M., Pietzsch, T., Preibisch, S., Rueden, C., Saalfeld, S., Schmid, B., Tinevez, J.Y., White, D.J., Hartenstein, V., Eliceiri, K., Tomancak, P., and Cardona, A. (2012). Fiji: An open-source platform for biological-image analysis. Nat. Methods *9*, 676–682.

Schulz, J.M., Redgrave, P., Mehring, C., Aertsen, A., Clements, K.M., Wickens, J.R., and Reynolds, J.N.J. (2009). Short-latency activation of striatal spiny neurons via subcortical visual pathways. J. Neurosci. *29*, 6336–6347.

Segev, R., Goodhouse, J., Puchalla, J., and Berry, M.J., 2nd (2004). Recording spikes from a large fraction of the ganglion cells in a retinal patch. Nat. Neurosci. *7*, 1154–1161.

Shamash, P., Carandini, M., Harris, K., and Steinmetz, N. (2018). A tool for analyzing electrode tracks from slice histology. bioRxiv. https://doi.org/10.1101/447995.

Shang, C., Liu, Z., Chen, Z., Shi, Y., Wang, Q., Liu, S., Li, D., and Cao, P. (2015). A parvalbumin-positive excitatory visual pathway to trigger fear responses in mice. Science *348*, 1472–1477.

Shang, C., Chen, Z., Liu, A., Li, Y., Zhang, J., Qu, B., Yan, F., Zhang, Y., Liu, W., Liu, Z., et al. (2018). Divergent midbrain circuits orchestrate escape and freezing responses to looming stimuli in mice. Nat. Commun. *9*, 1232.

Sparks, D.L. (2002). The brainstem control of saccadic eye movements. Nat. Rev. Neurosci. *3*, 952–964.

Steinmetz, N.A., Zatka-Haas, P., Carandini, M., and Harris, K.D. (2019). Distributed coding of choice, action and engagement across the mouse brain. Nature *576*, 266–273.

Storchi, R., Milosavljevic, N., Allen, A.E., Zippo, A.G., Agnihotri, A., Cootes, T.F., and Lucas, R.J. (2020). A High-Dimensional Quantification of Mouse Defensive Behaviors Reveals Enhanced Diversity and Stimulus Specificity. Curr. Biol. *30*, 4619–4630.e5.

Stringer, C., Pachitariu, M., Steinmetz, N., Reddy, C.B., Carandini, M., and Harris, K.D. (2019). Spontaneous behaviors drive multidimensional, brainwide activity. Science *364*, eaav7893.

Szekely, G.J., and Rizzo, M.L. (2005). Hierarchical clustering via joint between-within distances: extending Ward's minimum variance method. J. Classif. *22*, 151–183.

Takahashi, T. (1985). The organization of the lateral thalamus of the hooded rat. J. Comp. Neurol. *231*, 281–309.

Taniguchi, H., He, M., Wu, P., Kim, S., Paik, R., Sugino, K., Kvitsiani, D., Fu, Y., Lu, J., Lin, Y., et al. (2011). A resource of Cre driver lines for genetic targeting of GABAergic neurons in cerebral cortex. Neuron *71*, 995–1013.

Viskaitis, P., Irvine, E.E., Smith, M.A., Choudhury, A.I., Alvarez-Curto, E., Glegola, J.A., Hardy, D.G., Pedroni, S.M.A., Paiva Pessoa, M.R., Fernando, A.B.P., et al. (2017). Modulation of SF1 Neuron Activity Coordinately Regulates Both Feeding Behavior and Associated Emotional States. Cell Rep. *21*, 3559–3572.

Wei, P., Liu, N., Zhang, Z., Liu, X., Tang, Y., He, X., Wu, B., Zhou, Z., Liu, Y., Li, J., et al. (2015). Processing of visually evoked innate fear by a non-canonical thalamic pathway. Nat. Commun. *6*, 6756.

Weitz, A.J., Fang, Z., Lee, H.J., Fisher, R.S., Smith, W.C., Choy, M., Liu, J., Lin, P., Rosenberg, M., and Lee, J.H. (2015). Optogenetic fMRI reveals distinct, frequency-dependent networks recruited by dorsal and intermediate hippocampus stimulations. Neuroimage *107*, 229–241.

Whyland, K.L., Slusarczyk, A.S., and Bickford, M.E. (2020). GABAergic cell types in the superficial layers of the mouse superior colliculus. J. Comp. Neurol. *528*, 308–320.

Wilson, J.S., Hull, C.D., and Buchwald, N.A. (1983). Intracellular studies of the convergence of sensory input on caudate neurons of cat. Brain Res. *270*, 197–208.

Wolf, A.B., Lintz, M.J., Costabile, J.D., Thompson, J.A., Stubblefield, E.A., and Felsen, G. (2015). An integrative role for the superior colliculus in selecting targets for movements. J. Neurophysiol. *114*, 2118–2131.

Yekutieli, D., and Benjamini, Y. (2001). The control of the false discovery rate in multiple testing under dependency. Ann. Stat. *29*, 1165–1188.

Yger, P., Spampinato, G.L.B., Esposito, E., Lefebvre, B., Deny, S., Gardella, C., Stimberg, M., Jetter, F., Zeck, G., Picaud, S., et al. (2018). A spike sorting toolbox for up to thousands of electrodes validated with ground truth recordings in vitro and in vivo. eLife *7*, e34518.

Yilmaz, M., and Meister, M. (2013). Rapid innate defensive responses of mice to looming visual stimuli. Curr. Biol. *23*, 2011–2015.

Zeng, H., and Sanes, J.R. (2017). Neuronal cell-type classification: challenges, opportunities and the path forward. Nat. Rev. Neurosci. *18*, 530–546.

Zhang, Z., Liu, W.Y., Diao, Y.P., Xu, W., Zhong, Y.H., Zhang, J.Y., Lazarus, M., Liu, Y.Y., Qu, W.M., and Huang, Z.L. (2019). Superior Colliculus GABAergic Neurons Are Essential for Acute Dark Induction of Wakefulness in Mice. Curr. Biol. *29*, 637–644.e3.

STAR★METHODS

KEY RESOURCES TABLE

REAGENT or RESOURCE	SOURCE	IDENTIFIER
Antibodies		
Rabbit anti-GFP	Thermo Fisher Scientific	Cat# A-11122; RRID: AB_221569
Rabbit anti-parvalbumin	Abcam	Cat# ab11427; RRID: AB_298032
Rabbit anti-CamkII	Abcam	Cat# ab5683; RRID: AB_305050
Chicken anti-mCherry	Novus	Cat# NBP2-25158; RRID: AB_2636881
Rabbit anti-mCherry	Rockland	Cat# 600-401-379; RRID: AB_2209751
Alexa488 donkey anti-rabbit	Thermo Fisher Scientific	Cat# A-21206; RRID: AB_2535792
Alexa555 goat anti-rabbit	Thermo Fisher Scientific	Cat# A-21428; RRID: AB_2535849
Cy3 donkey anti-chicken	ImmunoJackson	Cat# 703-166-155 RRID: AB_2340364
DAPI	Roche	Cat# 10276236001
Bacterial and virus strains		
AAV virus: pAAV-hSyn-hM4D(Gi)-mCherry (AAV2)	Addgene	5047
AAV virus: AAV2/CamkII-hChr2(E123T/T159C)-p2A-EYFP-WPRE	UNC vector core	AV5456B
AAV virus: AAV2-hSyn- EYFP	UNC vector core	AV4376E
Chemicals, peptides, and recombinant proteins		
10x PBS	VWR	Cat# 437117K
1x PBS	VWR	Cat# 444057Y
Histofix 4%	Roche	Cat# P087.5
Sodium Azide (NaN_3)	Sigma	Cat# S2002-100G
Triton X-100	Sigma	Cat# S8875
Normal Donkey Serum	Millipore	Cat# 30-100ML
ProLong® Gold Antifade Mounting Medium	Thermo Fisher Scientific	Cat# P36934
Lipophilic tracer DiD	Thermo Fisher Scientific	Cat# D7757
Sodium Chloride (NaCl)	Sigma	Cat# S7653-250G
Potassium Chloride (KCl)	Sigma	Cat# P5405-25G
Calcium Chloride ($CaCl_2$)	Sigma	Cat# C5670-100G
Magnesium Chloride ($MgCl_2$)	Sigma	Cat# 4880
D-glucose (Dextrose)	Sigma	Cat# D9434-250G
Sodium phosphate monobasic (NaH_2PO_4)	Sigma	Cat# S5011
Sodium Hydroxide (NaOH)	Sigma	Cat# 655104-500G
Sodium bicarbonate ($NaHCO_3$)	Sigma	Cat# S8875-1KG
Buprenorphine	Ceva	Vetergesic
Surgical tissue adhesive	3M	Vetbond
Antibiotic (Cefazolin)	Sandoz	Cefazoline 1g
Dexamethasone	Dechra	Rapidexon 2mg/ml
Ketamine	Dechra	Nimatek 100mg/ml
Xylazine	VMD	XYL-M 2%
Superbond C&B Catalyst	Prestige-dental	7110
Superbond Quick Monomer	Prestige-dental	7111-100
Superbond C&B Polymer L-Radiopaque	Prestige-dental	7112-350
Experimental models: Organisms/strains		
C57BL/6 mouse line	The Jackson laboratory	JAX:000664
$Pvalb^{Cre}$ mouse line	The Jackson laboratory	JAX:008069

(*Continued on next page*)

Continued

REAGENT or RESOURCE	SOURCE	IDENTIFIER
Ntsr1-GN209^{Cre} mouse line	Laboratory of Keisuke Yonehara	Genset: 030780-UCD
Ai32 mouse line	The Jackson laboratory	JAX: 012569
Ai9 mouse line	The Jackson laboratory	JAX:007909
Gad2^{Cre} mouse line	The Jackson laboratory	JAX: 10802
Software and algorithms		
Fiji	Schindelin et al., 2012	RRID:SCR_002285
MATLAB	Mathworks	RRID:SCR_001622
Zen lite	Zeiss	N/A
t-distributed Stochastic Neighbor Embedding	Maaten and Hinton, 2008	N/A
SpikeGLX	NA	https://billkarsh.github.io/SpikeGLX/
GNU Octave	Free Software Foundation	www.gnu.org/software/octave
Psychophysics Toolbox	Psychtoolbox	http://psychtoolbox.org
SpyKING CIRCUS	Yger et al., 2018	https://spyking-circus.readthedocs.io/en/latest/
Phy	Cortex Lab at University College London	https://phy.readthedocs.io/en/latest/; https://github.com/cortex-lab/phy
WaveSurfer (version: 0.918)	Janelia Research Campus	https://wavesurfer.janelia.org/
ScanImage	Vidrio Technoloies	http://scanimage.vidriotechnologies.com/display/SIH/ScanImage+Home
Allen CCF Tools	Shamash et al., 2018	https://github.com/cortex-lab/allenCCF
TREES toolbox	Cuntz et al., 2010	https://github.com/cuntzlab/treestoolbox
Bonsai	Lopes et al., 2015	https://bonsai-rx.org/
DeepLabCut	Mathis et al., 2018	http://mackenziemathislab.org/deeplabcut
Other		
Wiretrol® II capillary micropipettes	Drumond Scientific	Cat# 5-000-2005
Laser-Based Micropipette Puller	Sutter Instrument	Cat# P-2000
Small Animal Stereotaxic Workstation	Narishige	Cat# SR-5N
Stereotaxic Micromanipulator	Narishige	Cat# SM-15R
Hydraulic Oil Micromanipulator	Narishige	Cat# MO-10
Oil Microinjector	Narishige	Cat# IM-9B
780 nm LED light source	Thorlabs	Cat# M780L3
Zeiss LSM 710 confocal microscope	Zeiss	Cat# LSM710
Neuropixels phase 3A system	Imec	N/A
FPGA Kintex-7 KC705	Xilinx	EK-K7-KC705-G
Micromanipulator	Sensapex	Cat# uMp-1
473 nm DPSS laser	Laserglow Tech	R471003GX LabSpec
Optic fiber cannulas	doriclenses	MFC_200/245-0.37_3.5mm_ZF1.25_FLT
Ferrule Patch Cable	Thorlabs	M83L01
Ferrule Rotary Joint Patch Cable	Thorlabs	RJPFL2
Ultrasound scanner Vantage 128	Verasonics	https://verasonics.com/vantage-systems/
High-frequency ultrasound probe L22v14	Verasonics	https://verasonics.com/high-frequency-linear-arrays/
Real-time fUSI data processing and display	AUTC	https://fusi-functional-ultrasound-imaging.com
microprecision motor	Zaber	X-LRM-DE

RESOURCE AVAILABILITY

Lead contact

Further information and requests for resources should be directed to and will be fulfilled by the lead contact, Karl Farrow (karl.farrow@nerf.be).

Materials availability

This study did not generate new unique reagents.

Data and code availability

The data and code generated during this study are available from the Lead Contact, Karl Farrow (karl.farrow@nerf.be) upon reasonable request.

EXPERIMENTAL MODEL AND SUBJECT DETAILS

Animals

All experimental procedures were approved by the Ethical Committee for Animal Experimentation (ECD) of the KU Leuven and followed the European Communities Guidelines on the Care and Use of Laboratory Animals (004–2014/EEC, 240–2013/EEC, 252–2015/EEC). Male and female adult (2-4 months old) transgenic mice were used in our experiments including, *Ntsr1-GN209Cre, Ai9, Thy1-STOP-YFP, Ai32 x Ntsr1-GN209Cre, Ai32 x PvalbCre and Ai32 x Gad2Cre. Ntsr1-GN209Cre* mice (Genset: 030780-UCD) express Cre recombinase in *Ntsr1-GN209* expressing neurons. *Ai9* (JAX: 007909) and *Thy1-STOP-YFP* (JAX: 005630) are reporter lines that express tdTomato and YFP fluorescent proteins, respectively, when in presence of the Cre recombinase. *Ai32* (JAX: 012569) is a reporter line that expresses Channelrhodopsin2 in presence of Cre recombinase. *PvalbCre* mice express Cre recombinase in parvalbumin-expressing neurons. *Gad2Cre* mice express Cre recombinase in *Gad2*-expressing neurons. Mice were kept on a 12:12 h light:dark cycle and sterilized food pellets and water were provided *ad libitum.* Experiments were performed during the light phase.

METHOD DETAILS

General surgical procedures

Anesthesia was induced at the beginning with an intraperitoneal injection of Ketamine (100 mg/kg) and Medetomidine (1 mg/kg). Before starting any surgical procedure, the paw of the animal was pinched to check for the absence of pedal reflex. After deep anesthesia was achieved, mice were placed in a stereotaxic workstation (Narishige, SR-5N), on a homeothermic blanket to keep a stable body temperature. Eye ointment was applied to protect the eyes from drying and from light (Dura tear, NOVARTIS, 288/28062–7) and Lidocaine (0.5%, 0.007 mg/g body weight) was injected under the skin above the skull. The surgical areas were shaved, and the skin was disinfected using iso-betadine. Then, the skin was cut following the midline and retracted to the sides to expose the skull. Anterior-posterior coordinates are measured from Bregma.

Viral injections

Once the skull was exposed, a hole was performed at the right coordinates by gently rotating a needle against the skull. We used micropipettes (Wiretrol II capillary micropipettes, Drumond Scientific, 5-000-2005) with an open tip of around 30 μm, prepared with a Laser-Based Micropipette Puller (Sutter Instrument, P-2000), and an oil-based hydraulic micromanipulator MO-10 (Narishige) for all stereotactic injections. To trace back the injection sites, we coated the glass pipette tip with DiD (Thermo, D7757).

For optogenetic experiments, we restricted the expression of channelrhodopsin2 (ChR2) to different cell classes by employing two strategies that have previously been used to study these same populations. First, to express ChR2 in NTSR, PV and GAD2 neurons, we crossed Cre-expressing transgenic mouse lines (NTSR-GN209-Cre, PV-Cre and GAD2-Cre) with a ChR2-reporter mouse line, Ai32 (Gale and Murphy, 2014; Gerfen et al., 2013; Madisen et al., 2010, 2012; Taniguchi et al., 2011). Second, we labeled CAMKII neurons of the retinorecipient layers of the colliculus by injecting wild-type mice with an adeno-associated virus (AAV2-CamkII-hChR2(E123T/T159C)-p2A-EYFP-WPRE; UNC vector core, AV5456B) that expresses ChR2 (Wei et al., 2015). We used *Ai9* and *Thy1-STOP-YFP* mice as wild-type mice. We injected 200–300 nL of AAV in 100 nL doses with a waiting time of 5–10 min after each injection. Coordinates for the superficial colliculus were AP: −3.6 to 3.8, ML: −0.2 to −0.3, DV: −1.1 to −1.4.

For chemogenetic experiments, we injected 300 nL of AAV2-hSyn-hM4D(Gi)-mCherry (Addgene, 50475), or AAV2-hSyn-EYFP (UNC vector core, AV4376E) as control, into the PPnT. PPnT coordinates: AP −3 to −3.4, ML −1.8 to 2, DV: −3.5 to −3.3.

Following injection, the skin was glued with Vetbond tissue adhesive (3M,1469) to close the wound. Next, mice were injected with painkillers (Buprenorphine 0.2 mg/kg I.P.) and antibiotics (Cefazolin 15 mg/kg I.P.) and were allowed to recover on top of a heating pad. After recovery from anesthesia, animals were provided with soft food and water containing antibiotics (emdotrim, ecuphar, BE-V23552) and were monitored for 3 days and administrated Buprenorphine and Cefazolin depending on the condition of the animal. Any following surgery was performed 21 days after injection to allow for proper gene expression.

Cranial windows and optic-fiber implantations

opto-fUSI

Once the mouse was anesthetized and the skull was exposed, the lateral and posterior muscles were retracted. Vetbond was applied to open skin and exposed muscle, and a titanium head plate was attached to the skull using dental cement (Superbond C&B, Prestige-dental). Then a cranial window extending over almost the whole extent of the left hemisphere and part of the right hemisphere (AP: +2 to −6.5mm, ML 1.5 to −4.5) was made with a drill. Then, an optic-fiber cannula (Doric Lenses, MF1.25, 200/245-0.37, FLT)

was implanted. The entry point of the fiber into the brain was AP: −3.6 to −3.8, ML +1.5 at a 56° angle. The fiber was slowly inserted 1.8 mm into the brain so that the tip would be placed at ML: 0 and DV: −1.1 to −1.2. Next, a ring of dental cement was formed around the craniotomy and the optic-fiber to stabilize the whole preparation. Finally, the cranial window was covered with silicone elastomer for protection and the mouse was allowed to recover on a heating pad. Mice were treated with painkillers (Buprenorphine 0.2 mg/kg I.P.), antibiotics (Cefazolin 15 mg/kg I.P.) and anti-inflammatory (Dexamethasone 0.1 mg/kg) drugs for 5 days.

For experiments where opto-fUSI and behavioral measurements were combined, the same protocol was followed but craniotomies expanded from ML −1.5 to −3.25.

In vivo *electrophysiology*

Once the mouse was anesthetized and the skull was exposed, Vetbond was applied to open skin and exposed muscle, and a titanium head plate was attached to the skull using dental cement (Superbond C&B, Prestige-dental). Then, cranial windows (∼0.5 to 1 mm^2) were performed over the coordinates of the target regions. The following coordinates were used as the center of craniotomies: SC: AP: −3.7, ML: −0.5; PPnT: AP: −3.3, ML: −1.9; lateral posterior nucleus of the thalamus: AP: −2.1, ML: −1.8; tail of caudate putamen: AP: −1.4, ML: −3.1. An additional hole was made for the implantation of an optic-fiber cannula. The entry point of the fiber into the brain was AP: −3.6 to −3.8, ML: +1.5 at a 56° angle. The fiber was slowly inserted 1.8 mm into the brain so that the tip would be placed at ML: 0 and DV: −1.1 to −1.2.

Behavioral tests

Opto-open field test

All behavioral experiments were performed in a custom made square wooden box (W: 50 cm x L: 50 cm x H: 36 cm). Dim ambient light (∼50 lux) was provided by a lamp (Paulmann Licht GmbH, PDG09/14) positioned above the arena and oriented away from it, toward a wall. Behavior was recorded at 30 fps using a camera (Point Grey Research, FMVU-03MTM-CS) positioned 53 cm above the center of the arena. For optogenetic activation we used a 473 nm DPSS laser system (Laserglow Technologies, R471003GX) connected to a patchcord with a rotatory joint (Thorlabs, RJPFL2). Optogenetic stimulation was controlled with custom software written in MATLAB. Before every experiment, the output of the laser was measured at 20 Hz or 50 Hz (2 ms pulse width) and set at 0.3-0.4 mW (9.5 – 12.5 mW/mm^2). For any given mouse line, a high-frequency stimulus was chosen based on preliminary behavioral data and the documented firing rates recorded in response to natural visual stimuli (Gale and Murphy, 2014, 2016; Hoy et al., 2019; Shang et al., 2015, 2018; Wei et al., 2015). In those mouse lines where 20 Hz stimulation did not evoke any visible response, the following experiments were done at 50 Hz. In the data shown here, CAMKII and NTSR mice were stimulated at 20 Hz whereas PV and GAD2 were stimulated at 50 Hz. We obtained similar results using either a 20 or 50 Hz (Figure 1) or 5 Hz (Figures S1I–S1N) stimulus. Control experiments were carried out with Cre-negative litter mates.

5 days after implantation of the optic fiber, mice were habituated to the handler, patchcord and experimental room for at least 3 days. The day of the test, mice were placed in the center of the arena and were allowed to freely explore for 2 min. After the acclimatization time, when the mice moved away (∼10 cm) from the perimeter of the box, toward the center, light stimulation was manually triggered. During any given test, mice were stimulated at high (20 Hz or 50 Hz, 20 or 50 pulses) and low (5 Hz, 20 pulses) frequencies in a pseudo-random manner. Time between stimuli was set to be of at least 30 s. A typical experiment lasted 20-40 min.

Repeated tests were always separated by at least 48h.

In tests that combined optogenetics with DREADDs, the experiments were performed as explained above, except that mice were injected with either CNO (2 mg/kg) or saline 30-40 min prior to the test and were only stimulated at 20Hz. To examine the role of the PPnT, all animals underwent five sessions separated by 48 hours except for Session 5, which took place 7 days after Session 4. Each animal was stimulated approximately 15 times in each 20 minutes session (16 ± 2 for hM4D animals, 15 ± 2 for controls).

Head-fixed tests

To assess the behavioral responses in head-fixed animals, mice were head-fixed on a custom 3d printed air-cushioned spherical treadmill (polystyrene white ball Ø 20cm). We recorded the movement of the ball using two motion sensors (Tindie, PMW3360). Eye and body movements of the mice were recorded using 2 cameras (frontal camera: Allied vision, mako G-030B + Lens: NAVITAR, HR F1.4/25MM; lateral camera: Allied vision, mako G-030B + Lens: Kowa, LMZ45T3) positioned at 25 cm (frontal) and 40 cm (lateral) from the mice head. Recording of the ball sensors and the cameras were triggered at the start of each trial and stopped and saved at the end of each trial. Stimulation time was confirmed using an LED that was triggered together with the laser and was placed behind the mouse (15cm) and recorded with the frontal camera. For the current work, only data from the lateral camera was used in the analysis.

Protocol of functional ultrasound imaging

5 days after surgery, mice were habituated to the handler, experimental room and to head-fixation on a platform for 7 days. All animals included in the fUSI experiments were tested for behavior (open field test) before each imaging session. Then, the awake mouse was head-fixed on the platform and the body movement was partially restrained by a foam shelter. The silicone cap was removed, and the cranial window was covered with a 2-3 % agarose layer to reduce brain movement. A 473 nm DPSS laser system was then connected to the optic fiber cannula using a ferrule patch cable (Thorlabs, M83L01). Before every experiment, the output of the laser was measured at 20 Hz or 50 Hz and set to 0.3-0.4 mW (9.5 – 12.5 mW/mm2). Next, acoustic gel (∼1 mL, Unigel, Asept) was applied on the agarose for ultrasound coupling and the ultrasound transducer (L22-14v, Verasonics) was lowered down to a distance of

~3 mm from the brain. The probe was moved along the lateral axis by a linear microprecision motor (Zaber, X-LRM-DE). At the beginning of each session, a reference anatomical scan was acquired for registration (53 sagittal planes from lateral +1.5 mm to −5 mm, 125 μm steps). Following, we acquired the functional scan (23 sagittal planes, from lateral +1.5 mm to −4.5 mm, 250 μm steps). Two optogenetic stimuli were applied at each plane (high and low frequencies) before moving to the next one. The parameters of the light stimulation were the same as those used during the behavioral experiments. For each stimulus, functional images were acquired for 20 s (10 Hz), and the stimulus was applied after a 10 s baseline. The functional imaging and optogenetic stimulation were controlled and synchronized using custom software written in MATLAB. Optogenetic stimuli consisted of a high (20 Hz, 20 pulses, 2 ms pulse width or 50 Hz, 50 pulses, 2 ms pulse width) and a low (5 Hz, 20 pulses, 2 ms pulse width, ~2 mW/mm^2) frequency stimulus. The acquisition of the 23 sagittal planes was acquired sequentially starting at lateral −4.5, and the whole craniotomy was imaged 7-12 times per session. Total acquisition time was ~3.5 h. Each mouse was imaged in 3 to 5 sessions separated by 48 to 72 hours.

opto-fUSI behavior protocol

A similar protocol as described above was used when imaging animals on a spherical treadmill. In this condition, we scanned 11 planes for registration (1 to 3.5 lateral, 125 μm steps) and used 7 sagittal planes (1.5 to 3.25 lateral, 250 μm steps) for the functional scan. A single stimulation (high frequency: NTSR = 20Hz, G2 = 50Hz; 1 s) was applied at each plane before moving to the next one. For each stimulus, functional images were acquired for 20 s (10 Hz), and the stimulus was applied after a 10 s baseline. The acquisition of the 7 sagittal planes was acquired sequentially starting at −1.5L, and the whole craniotomy was imaged 35 times in a single session. Total acquisition time was ~2.5 h.

Generation of a functional ultrasound image

This procedure was adapted from the sequence for fast, whole-brain functional ultrasound imaging described in Macé et al., 2018. An ultrasound probe containing a linear array of 128 ultrasound emitters/receivers, emitted plane waves (15 MHz, 2 cycles) in five different angles (−6°, −3°, 0°, 3°, 6°). The echoes from each plane wave were acquired with the receivers and adjusted with a time-gain compensation to account for the attenuation of ultrasound signals with depth (exponential amplification of 1 dB/mm). This process generated a single emit-receive image ('B-mode image') for each angle and was applied three times for averaging. The 15 individual B-mode images were then combined (~2 ms, 500 Hz), resulting in a higher quality image ('compound B-mode image').

50 compound B-mode images were acquired every 100 ms (10 Hz) to generate a functional ultrasound image. Blood cells flowing inside the vessels scatter back and shift the frequency of the emitted waves (Doppler effect). Such shifts were measured and extracted in real-time by a high performance computing workstation equipped with 4 GPUs (AUTC, Estonia), using singular-value-decomposition-based spatiotemporal filtering, and high-pass temporal filtering (cut-off frequency: 20 Hz). From the filtered data, we calculated the mean intensity of the Doppler signal (Power Doppler) in each voxel. Power Doppler integrates all the Doppler signals in a voxel to obtain an intensity value that is proportional to the amount of blood cells moving in that voxel at a given time. Unlike Color Doppler, it lacks information about velocity or direction of the blood flow but reliably reports hemodynamic changes in blood volume (Babcock et al., 1996; Macé et al., 2013; Rubin et al., 1994). The intensity value of a voxel at a given time was calculated as: $I(x,y) = A(x,y,t)^2$ where I is Power Doppler Intensity, x, y are the coordinates of a given voxel in a given plane, A is the amplitude of the compound B-mode images after filtering, and t was time. The resulting functional ultrasound image was 143 × 128 voxels in which each voxel had a size of 52.5 μm x 100 μm x 300 μm (Macé et al., 2018).

Electrophysiological recordings

12 *NTSR1-GN209-Cre x ChR2 (Ai32)* mice of either sex at the age of 2.5-3 months were used to record optogenetic and light driven responses in the superior colliculus and PAG (7 recordings), pulvinar (9 recordings), caudateputamen (9 recordings) and posterior paralaminar nuclei of the thalamus (3 recordings).

Two days after performing cranial windows, animals were habituated to the recording set up for 3–4 days. The day of the recording, head-posted animals were fixed on a treadmill or floating ball in front of a screen. Then, a Neuropixels probe phase 3A (Imec, Belgium) (Jun et al., 2017) coated with a fluorescent dye (DiD, Thermofisher) was inserted into the brain with the tip reaching down to 1-1.5 mm below the target area. Once the right depth was reached, it was left to rest for 20-30 min, before starting the recording. Artificial cerebrospinal fluid (150 mM NaCl, 5 mM K, 10 mM D-glucose, 2 mM NaH2PO4, 2.5 mM CaCl2, 1 mM MgCl2, 10 mM HEPES adjusted to pH 7.4 with NaOH) was used to cover the exposed brain and skull.

Neuropixel probes contain 960 recording sites on a single shaft distributed in two rows of 480 electrodes along 9600 μm (16 μm lateral spacing, 20 μm vertical spacing), of which 384 can be recorded simultaneously. In all our experiments, we recorded from the 384 electrodes closest to the tip, spanning 3840 μm. Signals were recorded at 30 kHz using the Neuropixels headstage (Imec), base station (Imec) and a Kintex-7 KC705 FPGA (Xilinx). High-frequencies (> 300 Hz) and low-frequencies (< 300 Hz) were acquired separately. To select the recording electrodes, adjust gain corrections, observe online recordings, and save data, we used SpikeGLX software. Timings of visual and optogenetic stimulation were recorded simultaneously using digital ports of the base station.

While recording from any given location, first, the superior colliculus of these mice received 30 repetitions of blue light trains (20 Hz, 20 pulses, 1 ms pulse width, 0.2 mW) spaced by 20 s intervals. Then, visual stimuli were presented.

Visual stimuli

Visual stimuli were presented on a 32-inch LCD monitor (Samsung S32E590C, 1920x1080 pixel resolution, 60 Hz refresh rate, average luminance of 2.6 cd/m^2) positioned perpendicular to the mouse head, at 35 cm from the right eye, so that the screen was covering 90° of azimuth and 70° of altitude of the right visual field. Visual stimuli were presented on a gray background (50% luminance), controlled by Octave (GNU Octave) and Psychtoolbox (Brainard, 1997; Pelli, 1997). The visual stimuli consisted of a small black disc that linearly expanded from 2° to 50° of diameter within 300 ms at the center of the screen and a disk of 50° diameter dimming from background to black within 300 ms. The stimuli were repeated 10 times.

Immunohistochemistry

Animals were perfused and post-fixed overnight using 4% paraformaldehyde (HistoFix, Roche). Vibratome sections (100-200 μm) were collected in 1x PBS and were incubated in blocking buffer (1x PBS, 0.3% Triton X-100, 10% Donkey serum) at room temperature for 1 hour. Then slices were incubated with primary antibodies in blocking buffer overnight at 4°C. The next day, slices were washed 3 times for 10 min each in 1x PBS with 0.3% Triton X-100 and incubated in secondary antibody solution diluted in blocking buffer overnight at 4°C. We used rabbit anti-GFP (Thermo Fisher, A-11122, 1:500) as a primary antibody to label ChR2-positive cells, anti-mCherry (Novus, NBP2-25158, 1:500) to label hM4D-postive cells. Alexa488 donkey anti-rabbit (Thermo Fisher, A21206, 1:500-1000) and Cy3 donkey anti-chicken (ImmunoJackson, 703-166-155, 1:1000) were used as secondary antibodies. Nuclei were stained with DAPI (Roche, 10236276001, 1:500) together with the secondary antibody solution. Sections were then again washed 3 times for 10 min in 1x PBS with 0.3% Triton X-100 and 1 time in 1x PBS, covered with mounting medium (Dako, C0563) and a glass coverslip. Confocal microscopy was performed on a Zeiss LSM 710 microscope. Images of areas with ChR2- and hMD4-expressing cells, the fiber location and the Neuropixels track labeled with DiD were obtained using a 10x (plan-APOCHROMAT 0.45 NA, Zeiss) objective.

Immunohistochemistry of overlapping markers

Selected tissue sections of 60 μm were obtained from 6 mice. We combined immunohistochemistry with crossed mouse lines and viral injections to check overlapping cell-types, namely: 1) for NTSR overlap with CAMKII or PV we used 1 *Ai9 x Ntsr1-GN209Cre* mouse and 3 *Ntsr1-GN209Cre* mice that were injected with an AAV expressing EYFP (AAV2-EF1a- DIO-hChR2(E123T/T159C)-p2A-EYFP- WPRE); 2) for overlap between GAD2 and PV we used 2 *Ai9 x Gad2Cre* mice; 3) and for PV overlapping with CAMKII we used 2 *Ai9 x PvalbCre* mice. We used the following primary antibodies to label different markers: rabbit anti-parvalbumin (abcam, ab11427, 1:1000-2000) to label parvalbumin positive cells, chicken anti-mCherry (Novus, NBP2-25158, 1:1000) and rabbit anti-mCherry (Rockland, 600-401-379, 1:1000) to label tdTomato positive cells, rabbit anti-CamkII (abcam, ab5683, 1:300-500) to label CAMKII positive cells. Alexa488 donkey anti-rabbit (Thermo Fisher, A21206, 1:500-1000), Alexa555 goat anti-rabbit (Thermo Fisher, A-21428, 1:1000) and Cy3 donkey anti-chicken (ImmunoJackson, 703-166-155, 1:1000), were used as secondary antibodies. The histochemistry procedure was the same as described in the previous Method details section. Stacks of optical images were obtained from 1-3 sections containing the superior colliculus using confocal microscope with 10x or 63x objective, for counting and example high-magnification images, respectively. Labeled cells were counted using the *Cell Counter* plugin of ImageJ software (ImageJ 1.53c, https://imagej.nih.gov/ij/). Cell bodies were determined by overlaying DAPI-stained nuclei with secondary antibody signal. The depth of each cell-type specific layer was analyzed in ImageJ by sampling distances in 4 places across the SCs from its surface to a visually assessed upper and lower margin of labeled cells.

QUANTIFICATION AND STATISTICAL ANALYSIS

All the statistical details of experiments can be found in the figure legends and results, including the statistical tests used, exact sample size and definition of significance. All values were calculated with Python or MATLAB. All the details concerning specific analysis are described below.

Analysis of behavioral data

Freely moving

Animal tracking was performed using DeeLabCut software (Mathis et al., 2018). Stimulus onsets and offsets were extracted with a custom-made Bonsai workflow (Lopes et al., 2015). Tracking data were sorted into peri-stimulus trials using custom made Python scripts. Trials where stimulation happened while the animal was at the very edge of the setup were not included in the analysis, unless explicitly stated. Behavioral parameters were calculated by pooling all trials per mouse and calculating the average, followed by averaging over mice. Speed was extracted based on positional data of the base of the tail obtained from DeepLabCut. Frames with probability lower than 0.9 were filtered out and linearly interpolated. Position data were smoothed with a median filter of window size = 5. The preferred body angle (Figure 1G) was obtained by first aligning the trajectories to the same initial position and by rotating them to cardinal x axis by an angel of their body position at the stimulus onset frame. The body position angle is the angle between the line connecting the tail base with the nose and the Cartesian x axis. Next, the preferred angle was calculated between then line of stimulus onset nose position and stimulus offset nose position. The whole-body drift was quantified as the perpendicular to the distance traveled in the first second relative to the axis of motion before the stimulus. Latency to the corner was analyzed as time needed to reach a corner (corner is defined as a square of 10 × 10 cm) after the stimulation onset.

Clustering analysis

The clustering of behavioral responses to the optogenetic stimulation is based on the approach used in Storchi et al. (2020). This approach enables an analysis of the distribution of behavioral responses for each mouse line in an unsupervised manner. DeepLabCut was used to track predefined body parts (nose, ears, proximal and distal ends of the tail). The following measures were calculated based on these body parts: locomotion (Loc), immobility (Imm), acceleration (Acc), lateral motility (LM) and lateral distance (LD) traveled. Locomotion measures the movement of the body center, while immobility measures the immobility of all tracked body parts. Lateral motion measures lateral displacement relative to the body orientation in the previous frame and to the orientation at the start of the stimulus. Lateral distance measures lateral movement of the animal relative to its orientation at the start of the optogenetic stimulation.

$$\text{i. } M(t) = T(t) - T(t - dt)$$

$$\text{ii. } R(t) = X_{nose} - X_{tail\_base}$$

$$\text{iii. } Loc(t) = \|M(t)\|_2$$

$$\text{iv. } Imm(t) = -\|X(t) - X(t - dt)\|_F$$

$$\text{v. } Acc(t) = Loc(t) - Loc(t - dt)$$

$$\text{vi. } LM(t) = O(t)\|M(t) - proj_{R(t-1)}(M(t))\|_2$$

$$\text{vii. } LD(t) = O(t)\|M(t) - proj_{R(0)}(M(t))\|_2$$

Where T the body position (average coordinate of all body parts excluding the tail end), X the coordinates of all body parts, $O \in \{-1, 1\}$ with O = 1 for rightward lateral movement and O = −1 for leftward lateral movement, and $proj_u(v)$ the orthogonal projection of v onto u. Lateral motility (LM) measures the lateral movement at timestep (M(t)) relative to the mouse orientation at the previous timestep $(R(t-1))$. Lateral distance (LD) measures the lateral movement relative to the mouse orientation at the start of the stimulation $(R(t-0))$. Each measure was normalized to maximally spread all values over the [0,1] interval. All the values from a measure were first ordered from low to high and replaced by their rank in this ordering. These ranks were subsequently normalized between 0 and 1. The responses for each measure were then concatenated for each trial and reduced to a 5-dimensional vector using sparse PCA. We then clustered the low-dimensional trial vectors using a Gaussian Mixture Model with K-Means initialization. Based on the Silhouette score and Davies-Bouldin criteria (Figure S1O), we chose 11 clusters. As some clusters had only a few trials, we subsequently performed a merging step which resulted in 6 final clusters. To merge clusters, we assigned each trial clusters that had less than 10 trials to the clusters with the next-highest posterior probability for each trial. This process continued until all clusters had 10 or more trials.

Head-fixed behavior

Pupil diameter and motion were extracted from the video recorded by the lateral camera shown in Figure S3B (right). The DeepLabCut toolbox was used to track 4 parts of the pupil: the upper, lower, left and right edges. As in the open-field behavior analysis, tracked part positions with a likelihood lower than 0.9 in a frame were linearly interpolated. The traces were smoothed with a Median filter of size 3. The pupil diameter was measured as the mean of the height and width of the pupil. The pupil motion was defined as the difference in position of the pupil, calculated as the mean position of the 4 tracked points. Both pupil diameter and motion were baseline subtracted. The baseline for the pupil diameter was set as the mean response 1 s before stimulation. Distance units in the video were estimated by recording an object of known size to find the scaling factor. The baseline for pupil motion was set as the pupil position at stimulation onset. The speed was measured as the pitching motion of the ball, where large positive values indicate a forward movement by the animal, 0 indicates no movement, and large negative values indicate backward movement. Trials were divided into running and still categories based on whether the mouse's mean running speed one second before stimulation exceeded predefined thresholds. If the mean pitch motion during the 1 s before stimulation exceeded the predefined upper threshold (9 a.u.), the trial was labeled a running trial. If the mean pitch motion was less than the predefined lower threshold (3 a.u.), the trial was labeled a still trial. Thresholds were set by the experimenter through visual inspection of the videos.

Analysis of fUSI data

Registration

At the beginning of each session, we acquired a reference anatomical map. These anatomical maps were then registered to the Allen Mouse Brain Common Coordinate Framework version 3 (CCFv3) (Allen Brain API; brain-map.org/api/index.html) (Figure 2D). Registration was done semi-automatically based on anatomical landmarks that could be recognized on both the anatomical map and CCFv3 (external outline of the brain, dorsal hippocampus, 3rd and 4th ventricles, cerebellar outline, middle cerebral sinus, colliculus, and corpus callosum). These landmarks were used to readjust the 3D volume of the reference map to the CCFv3 by applying scaling in either of the x, y, z axis and rotations and translations in the coronal, sagittal or axial planes when necessary. Then, we calculated the rotations and translations of the coronal, sagittal and axial planes to create a 3D transformation matrix (from anatomical map to CCFv3).

Segmentation

fUSI from each session were automatically registered to the CCFv3 using the 3D transformation matrices obtained in the previous steps. Assignment of voxels to brain areas was based on the CCFv3 segmentation. For our analysis, we excluded fiber tracts, ventricles, unsegmented parts of main brain structures (CTX, CTXsp, TH, HY, MB, HB, CB), merged layers of brain areas, and excluded or merged neighboring areas with volumes < 300 μm^3. Our final version of the atlas was comprised of 264 brain areas in one hemisphere of the brain (see Table S2).

Response time traces

The relative hemodynamic changes (ΔI/I) were calculated for each voxel, where I was the baseline (mean of 10 s before stimulus onset) and ΔI was the subtraction of the baseline to the signal at each time point. The traces of the individual areas were obtained from each trial by summing all the voxels assigned to each area (Figure 2E).

Data filtering and normalization

In order to analyze the response traces of each segmented area, first, we created a dataset with the temporal signals, Ti i = 1..Ntime, of each region, trial and session of each animal; $T_{animal\ repetition}(region, time)$. In this dataset, all the trials of the different sessions were added. Therefore, the repetitions were $N_{sessions} * N_{trials}$. The intensity signal obtained from the Power doppler is susceptible to brain tissue motions caused by the awake animal's movements. However, motion artifacts can typically be distinguished from hemodynamic changes based on the shape (noise/real; quick spiky/slow curved), and amplitude (noise/real ΔI/I; > 100%/1%–15%) of the signal. In this study, in order to remove trials affected by motion artifacts we computed the mean temporal signal of each region (Tm) and standard deviation (SD), and then eliminated outlier values where Ti-Tm were 2.5 times higher than the SD. The eliminated values were replaced by the previous non-eliminated value. To eliminate the global variations in the brain (baseline perturbations) we selected the 20% of the regions with lowest response during a 2 s time window after the stimulus onset, then averaged these regions to create a baseline signal. This baseline signal was then subtracted from all segmented areas. The resulting normalized temporal traces were used for statistical analysis (Figure 2G).

Active brain regions

To determine if a brain region was activated by a stimulus, first, we used the normalized temporal traces of every trial to calculate a T-score for each animal, using a general linear model, as commonly used in fMRI (Friston et al., 1995). To take into account the different temporal dynamics present in the responses, the GLM was applied using both 1 and 2 s windows stepped (0.5 s steps) from the beginning of the stimulus until 7.5 s after stimulus onset. Next, a one-sample two-tailed t test was performed on the n T-scores obtained for the n animals. The region was considered active if the resulting p value, adjusted for a false discovery rate (Benjamini and Hochberg FDR procedure), was < 0.05 (Figure S4D) (Benjamini and Hochberg, 1995). For display (such as in Figure 2J), we quantified the median response time courses across animals, we standardized the responses with regard to the values before stimulus onset (z-score) and we corrected for the relative differences between the stimulation levels of each animal. To do this we calculated a correction factor from normalizing the peak response (A = average of the signal 0.5 s around the maximal value within a time window after stimulus onset), across all brain areas where: $A_{norm(region)} = \frac{A(region)}{\sqrt{sum(A(region)^2)}}$, then divided each time point by the correction. The Average of all the corrected response traces, for each mouse line, are shown in Figures 2J and S2G and are used in the subsequent figures.

Pixel-to-pixel activity maps

To visualize pixel-to-pixel activity maps, for each voxel, we quantified the median of the response time courses across trials. We then standardized the responses computing the z-score, using the 10 s before stimulus onset and a 2 s time window after stimulus onset. Next, we averaged activity maps of animals belonging to the same mouse line applied a median filtering of 4 × 4 pixels on the resulting z-score map. The filtered z-score maps were used for visual inspection of the brain activity and for data visualization (Figure 5H).

Clustering of fUSI time courses

Time course of all active brain regions in the four neuronal groups were clustered using hierarchical classification and the e-linkage algorithm, an extensions of Ward's minimum variance method (Szekely and Rizzo, 2005). The optimal number of clusters was determined by inspection of the mean silhouette value (Rousseeuw, 1987) and Davies-Bouldin Index (Davies and Bouldin, 1979). Clustering was only preformed on the 1056 active areas for the 1 s optogenetic stimulus. Four clusters were finally included, namely: Fast, Delayed, Slow and Inhibitory, and can be described as follows. The Fast responses were characterized by a relatively fast rise time (1.27 ± 0.42 s), resulting in a transient response. The Delayed responses showed a clear delay with time to peak of

3.3 ± 0.79 s. The Slow responding areas started their responses early but took longer to reach their peak (2.1 s ± 0.70 s) and showed a more sustained response (1.78 ± 1.30 s). Finally, Inhibitory responses, showed a negative response. Inhibitory responses were preceded by a very transient early positive response (time-to-peak = 0.91 ± 0.65 s: decay time = 0.52 ± 0.18 s) in each cell-class except the GAD2 (Figures 3A and 3B).

Comparative network analysis

To assess the correlation between the functional responses either across the whole brain or within a predetermined group of areas, we calculated the Pairwise Pearson correlation coefficients between the mean response traces of the segmented areas during the 8 s after stimulus onset using the 'corrcoef' function in MATLAB.

Principal component analysis of the trajectories of the neuronal activity in 30 ''defensive'' brain areas was performed using the 'svd' MATLAB function.

Similarity matrices of the response properties of the different mouse lines or the similarity between correlation matrices was calculated measuring the Pairwise distance between each mouse line's mean responses (One minus the sample correlation between points), or between correlation matrices (One minus the sample Spearman's rank correlation between observations) using the 'pdist' function in MATLAB. To determine whether the differences in active brain regions were statistically significant, we performed a bootstrap analysis of whether the distance between evoked activity of different mouse lines was different from 0. To accomplish this, distributions were estimated using 1000 repetitions of random sampling of the evoked activity in individual mice. After correction for multiple comparisons (Yekutieli and Benjamini, 2001), p values were considered significant at alpha = 0.05.

Analysis of neuropixels recordings

Raw spiking activity

To extract spikes from raw Neuropixels data, the average voltage on each electrode in the 0.5 s before onset of the optogenetic stimulation was subtracted from the signal during stimulation. Spikes were identified using the 'findpeaks' function in MATLAB with a threshold of 4 standard deviations of the signal before the stimulation. Spikes during the 1 ms of each light pulse were excluded as they could cause artifacts, especially on the electrodes in the superior colliculus.

Activity maps

Confocal images of brain slices containing the probe tracks were aligned with the Allen Brain Atlas using the allen CCF tool (Shamash et al., 2018). This allowed us to identify the same slice of the fUSI dataset. To compare the activity on the probe with the fUSI signal, we averaged the z-scored fUSI signal (averaged across all stimulation repetitions and tested NTSR animals) of x-2 to x+2 pixels for each x location of the probe. The raw spiking data on the whole probe during the 4 s after each optogenetic stimulation was averaged across stimulations and resampled to match the spatial resolution of the fUSI data. We normalized each dataset separately to its maximal value, resulting in the plot shown in Figure 6G and analyzed in Figure 6F. Correlation coefficients were calculated using the 'corrcoef' function in MATLAB.

Spike sorting

The high-pass filtered in-vivo data was automatically sorted into individual units using SpyKING CIRCUS (Yger et al., 2018) with the following parameters: cc_merge = 0.95 (merging if cross-correlation similarity > 0.95), spike_thresh = 6.5 (threshold for spike detection), cut_off = 500 (cut-off frequency for the butterworth filter in Hz). Automated clustering was followed by manual inspection, merging of units if necessary and discarding of noise and multi-units using phy2 (https://github.com/cortex-lab/phy). Units were evaluated based on the average waveform shape and auto-correlogram. Only cells with < 1% of inter-spike intervals of $\leq$ 1 ms were considered and cross correlograms with nearby neurons were inspected to find spikes from the same neurons (Segev et al., 2004).

Detection of responding units

Peri-stimulus histograms (PSTH) were calculated using a bin size of 20 ms. For detection of responding cells and for plotting, the mean spikes/s during 0.3 (looming, dimming) or 0.5 s (optogenetic stimulus) before stimulus onset were subtracted from the cell's activity. We calculated a quality index to capture the reliability of a cell's response to the 10-30 stimulus repetitions. The quality index was defined as $QI = \frac{Var[\overline{C}_r]_t}{Var[C_t]_r}$ with C being the TxR response matrix, t = time dimension and r = repetition dimension (Baden et al., 2016). Cells were labeled as 'responding' if the maximal z-score during the stimulus exceeded 3 and if the quality index was at least 0.15.

Transiency measurements

For response transiency when stimulated with 20 light pulses (optogenetics), the mean response during the 40 ms after onset of each pulse was normalized to the absolute maximum of these 20 responses (positive or negative). The transiency of the response was defined as the area under the curve (AUC), i.e., the sum of these 20 values divided by 20. An AUC of 1 means that the cell responded equally well to all 20 pulses, an AUC of -1 means that the cell's activity was equally suppressed by each pulse.

Clustering optogenetically induced responses

We classified the responses to optogenetic stimulation measured with Neuropixels probes into the 4 fUSI clusters (fast, delayed, slow, inhibition). To achieve this, we extracted the peak firing rate for each of the 20 optogenetic stimuli, normalized these 20 measurements to the maximum response, and classified the normalized peak responses following a stepwise process:

1. Fast: Peak response needs to happen for the first stimulus, and the normalized response needs to drop below 0.52 after the third stimulus, and the response cannot drop below −0.1 (no strong inhibition).
2. Delayed: Peak happens later than the first stimulus, and the response for the second stimulus is < 0.72, and the response cannot drop below −0.1 (no strong inhibition).
3. Slow: Peak happens before the fourth stimulus, and the response cannot drop below −0.1 (no strong inhibition).
4. Inhibition: The average response after the eighth stimulus is < 0.